

Radiation Magnetohydrodynamic Simulations of Sub-Eddington Accretion Flows in AGN: Origin of Soft X-ray Excess and Rapid Time Variabilities

TAICHI IGARASHI,¹ YOSHIAKI KATO,² HIROYUKI R. TAKAHASHI,³ KEN OHSUGA,⁴ YOSUKE MATSUMOTO,¹ AND RYOJI MATSUMOTO¹

¹*Department of Physics, Graduate School of Science, Chiba University*

1-33 Yayoi-Cho, Inage-Ku

Chiba 263-8522, Japan

²*RIKEN*

2-1 Hirosawa, Wako

Saitama, 351-0198, Japan

³*Faculty of Arts and Sciences, Department of Natural Sciences, Komazawa University*

1-23-1 Komazawa, Setagaya

Tokyo, 154-8525, Japan

⁴*Center for Computational Sciences, University of Tsukuba*

1-1-1 Ten-nodai

Tsukuba 305-8577, Japan

ABSTRACT

We investigate the origin of the soft X-ray excess component in Seyfert galaxies observed when their luminosity exceeds 0.1% of the Eddington luminosity (L_{Edd}). The evolution of a dense blob in radiatively inefficient accretion flow (RIAF) is simulated by applying a radiation magnetohydrodynamic code, CANS+R. When the accretion rate onto a $10^7 M_{\odot}$ black hole exceeds 10% of the Eddington accretion rate ($\dot{M}_{\text{Edd}} = L_{\text{Edd}}/c^2$, where c is the speed of light), the dense blob shrinks vertically because of radiative cooling and forms a Thomson thick, relatively cool ($\sim 10^{7-8}$ K) region. The cool region coexists with the optically thin, hot ($T \sim 10^{11}$ K) RIAF near the black hole. The cool disk is responsible for the soft X-ray emission, while hard X-rays are emitted from the hot inner accretion flow. Such a hybrid structure of hot and cool accretion flows is consistent with the observations of both hard and soft X-ray emissions from ‘changing-look’ active galactic nuclei (CLAGN). Furthermore, we find that quasi-periodic oscillations (QPOs) are excited in the soft X-ray emitting region. These oscillations can be the origin of rapid X-ray time variabilities observed in CLAGN.

Keywords: accretion, accretion disks — galaxies: active — magnetohydrodynamics (MHD) — radiative transfer

1. INTRODUCTION

Active galactic nuclei (AGN) are categorized into low-luminosity AGN such as M87 and luminous AGN such as Seyfert galaxies. In low luminosity AGN, their luminosity L is less than 0.1% of the Eddington luminosity L_{Edd} . The broadband spectrum of electromagnetic radiation from low-luminosity AGN can be explained by radiatively inefficient accretion flows (RIAFs) onto a supermassive black hole (e.g., Narayan et al. 1995). RIAFs are optically thin, hot ($T \sim 10^{11}$ K), advection-dominated accretion flows in which the radiation energy is much smaller than the thermal energy. On the other hand, the optical-UV thermal radiation observed in luminous AGN is emitted by optically thick, cold ($T \sim 10^{4-5}$ K) disks. Such disks can be modeled by standard accretion disks (Shakura & Sunyaev 1973) driven by sub-Eddington accretion flows. A key parameter characterizing the activity of AGN is the ratio of their accretion rate \dot{M} to the Eddington accretion rate \dot{M}_{Edd} defined by $\dot{M}_{\text{Edd}} = L_{\text{Edd}}/c^2$, where c is the speed of light.

Abramowicz et al. (1995) showed that RIAFs can exist only when the accretion rate is less than 1-10% of the Eddington accretion rate. When the accretion rate of a RIAF exceeds this upper limit, radiative cooling dominates the viscous heating so that the RIAF cools and transitions to an optically thick, cold disk. Such transitions are observed in stellar-mass black holes as hard-to-soft state transitions (e.g., Fender et al. 2004). In AGN, it is expected that low-luminosity AGN evolve toward luminous AGN when the accretion rate exceeds the upper limit for RIAF. During this transition, accretion flow stays in an intermediate state between a RIAF and standard disks. The time evolution of such sub-Eddington accretion flows onto a supermassive black hole can be studied by radiation magnetohydrodynamic (RMHD) simulations.

Global three-dimensional magnetohydrodynamic (MHD) simulations of nonradiative accretion flows (e.g., Hawley 2000) showed that the mass accretion is driven by Maxwell stress enhanced by magnetic turbulence driven by magnetorotational instability (MRI). Machida et al. (2000) showed that magnetic fields enhanced by MRI buoyantly escape from the disk and form a magnetically active disk corona. Global two-dimensional RMHD simulations of black hole accretion flows have been initiated by Ohsuga et al. (2009) and Ohsuga & Mineshige (2011). Three-dimensional RMHD simulations have been performed for accretion flows with an accretion rate exceeding the Eddington accretion rate (e.g., Takahashi et al. 2016; Sadowski & Narayan 2015; Jiang et al. 2019b). Jiang et al. (2019a) presented the results of RMHD simulations for sub-Eddington accretion flows, but the accretion rate in their simulations is close to $\sim 1\dot{M}_{\text{Edd}}$. Numerical simulations for lower accretion rates but exceeding the upper limit for RIAFs are challenging because we need to resolve a cool disk.

Machida & Matsumoto (2008) carried out global three-dimensional MHD simulations of the nonradiative accretion flow infalling from the outer cool disk. They showed that when the cool matter infalls by losing angular momentum, an inner torus (or dense blob) is formed. Furthermore, they showed that the torus is deformed into a nonaxisymmetric shape due to the growth of the nonaxisymmetric instability (e.g., Papaloizou & Pringle 1984; Drury 1985). They also showed that quasi-periodic oscillations (QPOs) are excited in the inner torus. Figure 1(a) schematically shows a dense blob formed in the hot, low-density accretion flow. As the accretion rate from the outer cold disk increases, the blob density increases. When the density of the blob exceeds the upper limit for RIAF, the dense blob is subject to the cooling instability. Figure 1(b) schematically shows an intermediate state between low-luminosity AGN and luminous AGN (e.g., Noda et al. 2014; Sniegowska et al. 2020; Mahmoud & Done 2020). In the region where the cool blob is formed by cooling instability, soft X-rays are emitted (the green region in Figure 1(b)).

The radially stratified structure shown in Figure 1(b) is similar to the interface between the hot accretion flow and outer standard disk (e.g., Manmoto et al. 2000). It has been suggested that such a region can produce a low-frequency oscillation in black hole binaries (e.g., Mahmoud & Done 2018). For stellar-mass black holes, Machida et al. (2006) presented the results of global three-dimensional MHD simulations of the hard-to-soft state transition. By considering optically thin radiative cooling, they showed that when the surface density of the disk exceeds the upper limit for RIAF, the disk shrinks in the vertical direction by radiative cooling and forms a region with temperature 10^8 K outside the hot RIAF. They found that the azimuthal magnetic field is enhanced when the azimuthal component of the magnetic field is symmetric with respect to the equatorial plane of the disk. Because this azimuthal magnetic field supports the disk, the disk stays in the optically thin state. This intermediate state corresponds to the luminous hard state observed during the hard-to-soft state transition in stellar-mass black hole candidates. In addition, Oda et al. (2009, 2012) showed that when the azimuthal magnetic fields are considered, steady solutions of luminous hard-state disk exist even when the accretion rate exceeds the upper limit of RIAF. Machida et al. (2006) dismissed investigating further evolution because numerical instabilities grow in the magnetically dominated region. More importantly, they could not treat the optically thick region that is formed in the stage later than their simulations because they assumed optically thin radiative cooling.

Some AGN show transitions between type 1 with broad emission lines and type 2 without broad emission lines. Such transitions have been observed in Seyfert galaxies such as NGC2617 (e.g., Shappee et al. 2014), Mrk590 (e.g., Denney et al. 2014), Mrk1018 (Husemann et al. 2016; LaMassa et al. 2017; Noda & Done 2018), and NGC1566 (Parker et al. 2019; Oknyansky et al. 2019). Some quasars also show transitions between type 1 and type 2 (e.g., LaMassa et al. 2015; MacLeod et al. 2016), and these are called changing-look AGN (CLAGN). The transitions occur in the timescale of years, disfavoring the model of an external origin, such as occultation by a dust torus. CLAGN show soft X-ray time variations preceding the UV-optical intensity variations (Shappee et al. 2014; Oknyansky et al. 2017; Noda

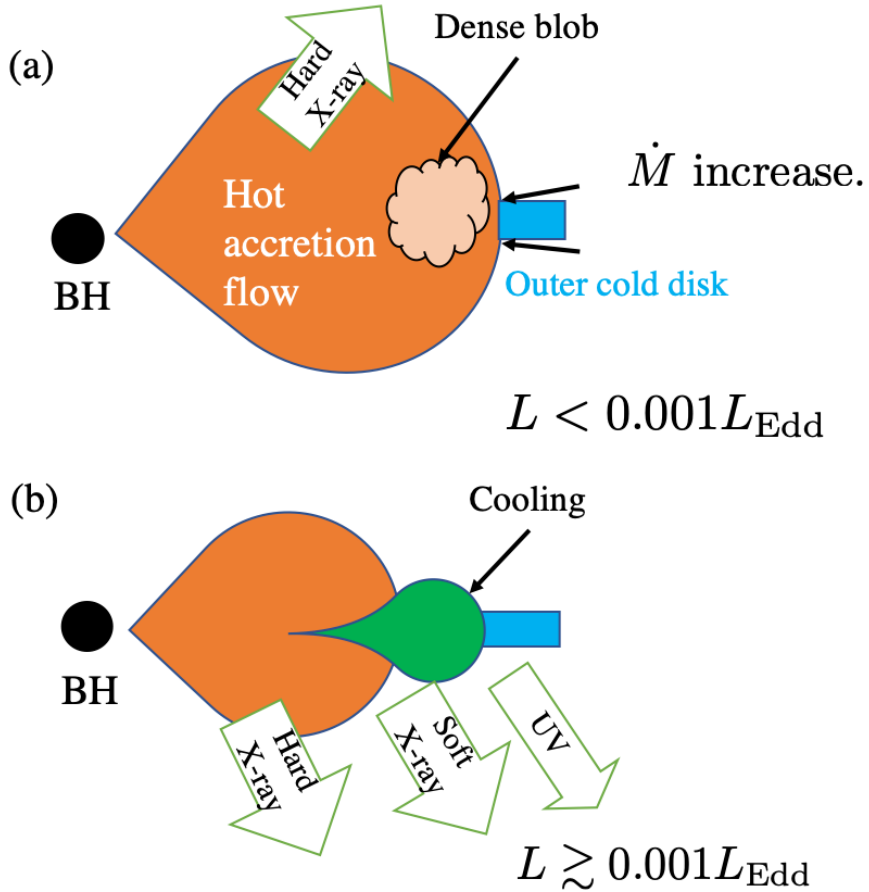


Figure 1. A schematic picture of the central engine of AGN during the hard-to-soft transition. Orange, green, and blue areas show hot RIAF, soft X-ray emitting region and outer UV emitting standard disks, respectively. (a) A dense blob is formed by an increase of the mass accretion rate, (b) when the luminosity exceeds $0.001 L_{\text{Edd}}$, a soft X-ray emitting region is formed by radiative cooling.

& Done 2018). They also indicate that the primary source of the time variation is the soft X-ray emission from the region near the supermassive black hole.

Previous studies have shown that the X-ray spectra of Seyfert galaxies become softer as their luminosity increases (e.g., Arnaud et al. 1985; Turner & Pounds 1989). Through a method of variability-assisted broadband spectroscopy, Noda et al. (2014) found that a highly variable soft X-ray excess component appears in NGC3227 when the source luminosity exceeds 0.1% of the Eddington luminosity. In contrast, Noda & Done (2018) showed that when the bolometric luminosity in Mrk1018 decreases below 1% of the Eddington luminosity, the soft X-ray excess disappears.

In this paper, we present the results of the RMHD simulation of the accretion flow when an overdense region appeared in RIAF, although the formation of such an overdense region in a realistic situation is left as an open question. We consider accretion flows with accretion rate $\sim 0.1 \dot{M}_{\text{Edd}}$. This mass accretion rate is an order of magnitude smaller than that in RMHD simulations reported by Jiang et al. (2019a). We report the time-evolution of the structure and variability of the overdense region.

2. METHOD

2.1. Basic Equations

Table 1. Units in this paper

| Units | Values |
|--------------------------|--|
| Length | $r_s = 3 \times 10^{12}$ cm |
| Velocity | $c = 3.0 \times 10^{10}$ cm/s |
| Time | $t_0 = r_s/c = 100$ s |
| Luminosity | $L_{\text{Edd}} = 4\pi cGM_{\text{BH}}/\kappa_{\text{es}} = 1.25 \times 10^{45}$ erg/s |
| Eddington accretion rate | $\dot{M}_{\text{Edd}} = L_{\text{Edd}}/c^2 = 1.4 \times 10^{24}$ g/s |
| Density | $\rho_0 = 2.0 \times 10^{-11}$ g/cm ³ |
| Magnetic Field | $B_0 = \sqrt{4\pi\rho_0 c^2} = 4.9 \times 10^5$ G |

We solve the RMHD Equations, which consist of resistive-magnetohydrodynamic Equations coupled with the 0th and 1st moments of radiation transfer Equations in cylindrical coordinates (r, φ, z) . General relativistic effects are considered using the pseudo-Newtonian potential (Paczynsky & Wiita 1980) $\phi_{\text{PN}} = -GM_{\text{BH}}/(R - r_s)$, where $M_{\text{BH}} = 10^7 M_{\odot}$ is the black hole mass, $R(= \sqrt{r^2 + z^2})$ is the distance from the black hole, $r_s(= 2GM_{\text{BH}}/c^2)$ is the Schwarzschild radius, and G is the gravitational constant.

The basic Equations are nondimensionalized by using normalizations shown in Table 1 and expressed as follows:

$$\frac{\partial \rho}{\partial t} + \nabla \cdot (\rho \mathbf{v}) = 0, \quad (1)$$

$$\frac{\partial \rho \mathbf{v}}{\partial t} + \nabla \cdot (\rho \mathbf{v} \mathbf{v} + p_t \mathbf{I} - \mathbf{B} \mathbf{B}) = -\rho \nabla \phi_{\text{PN}} - \mathbf{S}, \quad (2)$$

$$\frac{\partial E_t}{\partial t} + \nabla \cdot [(E_t + p_t) \mathbf{v} - \mathbf{B}(\mathbf{v} \cdot \mathbf{B})] = -\nabla \cdot (\eta \mathbf{j} \times \mathbf{B}) - \rho \mathbf{v} \cdot \nabla \phi_{\text{PN}} - cS_0, \quad (3)$$

$$\frac{\partial \mathbf{B}}{\partial t} + \nabla \cdot (\mathbf{v} \mathbf{B} - \mathbf{B} \mathbf{v} + \psi \mathbf{I}) = -\nabla \times (\eta \mathbf{j}), \quad (4)$$

$$\frac{\partial \psi}{\partial t} + c_{\text{h}}^2 \nabla \cdot \mathbf{B} = -\frac{c_{\text{h}}^2}{c_{\text{p}}^2} \psi, \quad (5)$$

where ρ , \mathbf{v} , \mathbf{B} , and $\mathbf{j} = \nabla \times \mathbf{B}$ are the mass density, velocity, magnetic field, and current density, respectively. In addition, $p_t = p_{\text{gas}} + B^2/2$ is the total pressure, and $E_t = \rho v^2/2 + p_{\text{gas}}/(\gamma - 1) + B^2/2$ is the total energy, where $\gamma = 5/3$ is the specific heat ratio. We apply the so-called anomalous resistivity:

$$\eta = \begin{cases} \eta_0 \min [1, (v_d/v_c - 1)^2], & v_d \geq v_c \\ 0, & v_d \leq v_c \end{cases} \quad (6)$$

where $\eta_0 = 0.01cr_s$, $v_c = 0.9c$, and $v_d = jm_p/(\epsilon\rho)$ are the upper limit of the resistivity, critical velocity, and drift velocity, respectively. Here m_p is the proton mass and e is the electron charge. The resistivity η becomes large when the drift velocity v_d exceeds the critical velocity v_c (e.g., Yokoyama & Shibata 1994). In Equations (4) and (5), ψ is introduced so that the divergence-free magnetic field is maintained within minimal errors during time integration where c_{h} and c_{p} are constants (see Matsumoto et al. 2019, for more details).

In Equations (2) and (3), \mathbf{S} and S_0 are the radiation momentum and the radiation energy source terms, respectively, and are derived by solving the frequency-integrated 0th and 1st moments of the radiation transfer Equations expressed in the following forms (see Lowrie et al. 1999; Takahashi et al. 2013; Takahashi & Ohsuga 2013; Kobayashi et al. 2018):

$$\frac{\partial E_r}{\partial t} + \nabla \cdot \mathbf{F}_r = cS_0, \quad (7)$$

$$\frac{1}{c^2} \frac{\partial \mathbf{F}_r}{\partial t} + \nabla \cdot \mathbf{P}_r = \mathbf{S}, \quad (8)$$

where

$$S_0 = \rho \kappa_{\text{ff}}(a_r T^4 - E_r) + \rho(\kappa_{\text{ff}} - \kappa_{\text{es}}) \frac{\mathbf{v}}{c} \cdot [\mathbf{F}_r - (\mathbf{v} E_r + \mathbf{v} \cdot \mathbf{P}_r)], \quad (9)$$

Table 2. Parameters adopted in this paper.

| Parameters | Values |
|---|---|
| Radial dependence of angular momentum | $a = 0.46$ |
| Radius at the initial density maximum | $r_0 = 40r_s$ |
| Initial plasma β around the density maximum | $\beta = 10$ |
| Sound speed of the disk | $c_{s0} = 5.6 \times 10^{-3}c$ |
| Sound speed of the corona | $c_{sc} = 0.9c$ |
| Gas pressure at the initial density maximum | $p_0 = \rho_0 c_{s0}^2 = 6.0 \times 10^5 \text{ g/cm}^2/\text{s}$ |
| Ratio of the density of the corona to the disk | $\rho_{c0}/\rho_0 = 7 \times 10^{-6}$ |
| Black hole mass | $M_{\text{BH}} = 10^7 M_\odot$ |

$$\mathbf{S} = \rho \kappa_{\text{ff}} \frac{\mathbf{v}}{c} (a_r T^4 - E_r) - \rho (\kappa_{\text{ff}} + \kappa_{\text{es}}) \frac{1}{c} [\mathbf{F}_r - (\mathbf{v} E_r + \mathbf{v} \cdot \mathbf{P}_r)]. \quad (10)$$

In Equations (9) and (10), $\kappa_{\text{ff}} = 1.7 \times 10^{-25} m_p^{-2} \rho T^{-7/2} \text{ cm}^2/\text{g}$ is the free-free absorption opacity where $\kappa_{\text{es}} = 0.4 \text{ cm}^2/\text{g}$ is the electron scattering opacity. The gas temperature, T , is related to the gas pressure and density by $p_{\text{gas}} = \rho k_B T / (\mu m_p)$, where k_B , and $\mu = 0.5$ are the Boltzmann constant and mean molecular weight, respectively. In this paper, we mainly study the region with temperature higher than 10^7 K . For more realistic simulations of AGN accretion flows including the lower temperature region, we have to consider the opacity of metals (e.g., Jiang et al. 2019a,b).

The MHD part of the RMHD Equations is solved by CANS+ (Matsumoto et al. 2019), which adopts the HLLD approximate Riemann solver (Miyoshi & Kusano 2005), fifth-order monotonicity-preserving interpolation scheme (Suresh & Huynh 1997), and hyperbolic divergence cleaning method for solving the induction Equation (Dedner et al. 2002). The simulation code for the radiation part is the same as Kobayashi et al. (2018), and the moment Equations of the radiative transfer are solved with the M1-closure relation (González et al. 2007; Takahashi et al. 2016, and references therein). Our RMHD code is referred to as CANS+R hereafter.

2.2. Initial condition and boundary conditions

We simulate the AGN accretion flows shown in Figure 1. It is desirable to include the outer cold disk and study the evolution of the inner region when the accretion rate from the outer cold disk increases. In CLAGN, however, the time scale of the increase of the mass accretion rate that triggers the state transition of the inner region is several years. This time scale is much longer than the time scale for which we can carry out global three-dimensional simulations including the region near the black hole. Thus, we do not include the outer cold disk in the simulation region. Instead, we start from a nonaccreting disk with temperature $T \sim 10^8 \text{ K}$ and simulate the evolution of the disk without including the radiative cooling until the disk is heated by accretion driven by the angular momentum transport by MRI.

It should be noted that we do not simulate the origin of the increase of the accretion rate from the outer region, inducing the state transition in the inner region. Instead, we study the evolution of the density enhancement produced by the accretion from the cold disk.

For the initial condition, we set an equilibrium model of a rotating disk assuming a polytropic equation of state, $p = K \rho^{1+1/n}$ with $n = 3$, and power-law specific angular momentum distribution, $l = l_0 (r/r_0)^a$ with $l_0 = \sqrt{GM r_0^3 / (r_0 - r_s)^2}$, where r_0 is the radius of the density maximum of the disk. The initial density and gas pressure of the disk are given by

$$\rho_d = \rho_0 \left(1 - \frac{\gamma}{c_{s0}^2} \frac{\tilde{\phi} - \tilde{\phi}_0}{n+1} \right)^n \quad (11)$$

and

$$p_d = p_0 \left(\frac{\rho_d}{\rho_0} \right)^{1+\frac{1}{n}} \quad (12)$$

respectively, where ρ_0 , c_{s0} and $p_0 = \rho_0 c_{s0}^2 / \gamma$ are the initial density, sound speed and gas pressure of the disk at $(r, z) = (r_0, 0)$, respectively. The potential $\tilde{\phi}$ is the effective potential calculated by

$$\tilde{\phi} = \phi + \frac{1}{2(1-a)} \left(\frac{l}{r} \right)^2. \quad (13)$$

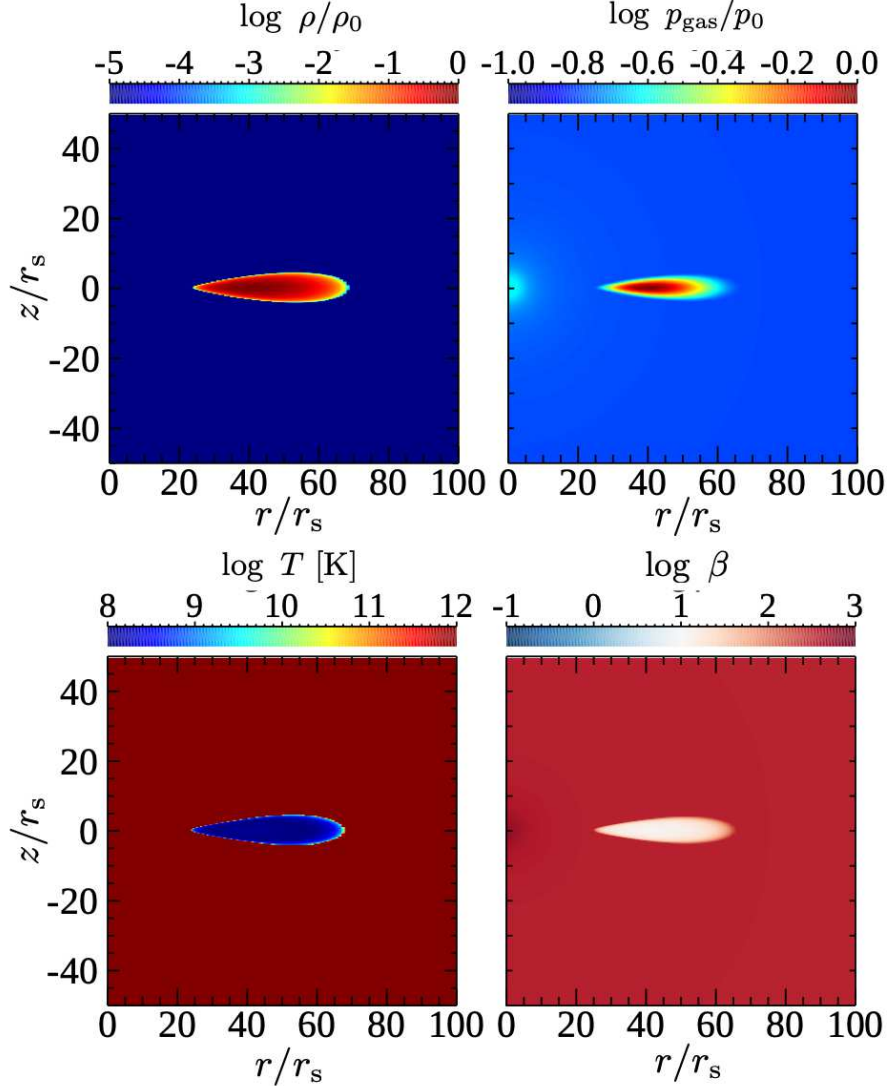


Figure 2. Distribution of gas density (upper left), gas pressure (upper right), gas temperature (lower left), and plasma β (lower right) in the poloidal plane at $t = 0$.

In Equation (11), $\tilde{\phi}_0 = \tilde{\phi}(r_0, 0)$. Outside the disk, we assumed a spherical, isothermal and static corona with temperature $T \sim 10^{12}$ K. The density and pressure distribution of the corona are given by

$$\rho_c = \rho_{c0} \exp\left(-\frac{\phi - \phi_0}{c_{sc}^2/\gamma}\right) \quad (14)$$

and

$$p_c = \rho_c c_{sc}^2/\gamma = p_{c0}(\rho_c/\rho_{c0}) \quad (15)$$

respectively, where ρ_{c0} , p_{c0} , and ϕ_0 are the coronal density, gas pressure and potential at $(r, z) = (r_0, 0)$, respectively, and c_{sc} is the constant sound speed in the corona. The pressure ratio of corona to disk is $p_{c0}/p_0 \sim 0.18$ at $(r, z) = (r_0, 0)$.

A weak, purely poloidal magnetic field is embedded in the initial disk. The initial magnetic field distribution is described in terms of the φ -component of the vector potential A_φ , which is assumed to be proportional to the density ($A_\varphi \propto \rho$) and r . The strength of the magnetic field is parametrized by the ratio of the gas pressure to the magnetic pressure (plasma β) that is assumed to be constant in the initial disk. Table 2 shows the parameters adopted in the simulation we report in this paper.

Figure 2 shows the distribution of initial gas density (upper left), gas pressure (upper right), temperature (lower left), and plasma- β (lower right) in the poloidal plane at $t = 0$. The half thickness of the disk is $\sim 5r_s$, and the inner edge of the disk is $r \sim 25r_s$. The minimum temperature of the disk is $T \sim 10^8$ K. These initial conditions are the same as Kato et al. (2004) (see also Hawley & Balbus 2002).

The computational domain of our simulation is $0 \leq r < 274r_s$, $0 \leq \varphi < 2\pi$, and $|z| < 233r_s$; and the number of grid points is $(n_r, n_\varphi, n_z) = (592, 32, 704)$. Grid spacing is $0.1r_s$ in the radial and vertical directions when $r < 20r_s$ and $|z| < 5r_s$ and increases outside the region. The absorbing boundary condition is imposed at $R = 2r_s$, and the outer boundaries are free boundaries where waves can be transmitted.

3. RESULTS

We avoided including radiative cooling until the disk is heated by accretion. We carried out numerical simulations without including radiative cooling until RIAF is formed. In Section 3.1, we present the results of such simulations. After quasi-steady RIAF is formed, we specify the initial density of the disk ρ_0 and carry out simulations considering the radiation process. When the density exceeds the upper limit for the existence of RIAF, cooling instability grows. The results of such simulations are presented in Section 3.2. We note that in AGN, the density of RIAF increases as the mass accretion rate from the outer cold disk increases. Cooling instability grows in local regions where the density exceeds the threshold. In Section 3.3, we show that QPOs are excited as a result of the growth of the cooling instability.

3.1. Formation of MHD accretion flow

During the time range $0 < t < t_c = 1.58 \times 10^4 t_0$, which equals seven Keplerian rotation periods at the density maximum of the initial disk at $r = r_0$, we ignored all radiation processes and followed the evolution of the nonradiative accretion flow until quasi-steady state is attained as a result of the growth of the MRI.

Figure 3 is the same as Figure 2 but at $t = t_c$. Because of the angular momentum transport by Maxwell stress is enhanced by MRI, the initial disk spreads and the density becomes nearly flat in the radial direction up to $r = 80r_s$. The disk is heated to $T \gtrsim 10^9$ K by releasing gravitational energy and the disk expands in the vertical direction. Gas pressure is dominant inside the disk, but plasma β becomes low in the disk corona where magnetic fields buoyantly escape from the disk.

Figure 4 shows the radial distribution of surface density, gas temperature, and gas pressure at $t = 0$ (dashed curves) and at $t = t_c$ (solid curves). The surface density Σ is calculated from

$$\Sigma = \int_{-10r_s}^{10r_s} \rho dz. \quad (16)$$

The radial distribution of the surface density shown in Figure 4(a) is nearly proportional to $r^{0.5}$. This radial dependence ($\Sigma \propto r^{0.5}$) is the same as the convection-dominated accretion flow (CDAF, see e.g., Quataert & Gruzinov 2000). Machida et al. (2001) showed that the radial dependence of density and other quantities of nonradiative MHD accretion flow are almost the same as CDAF in which $\rho \propto r^{-0.5}$, $T \propto r^{-1}$ and $p_{\text{gas}} \propto r^{-1.5}$. The radial distribution of the temperature (Figure 4(b)) is slightly steeper than the CDAF solution. Inside the radius of the density maximum of the initial disk ($r < r_0$), the accretion flow is approaching the solution of nonradiative MHD accretion flows. We should note, however, that a small enhancement of surface density remains around $r = r_0$.

In this paper, we study the evolution of the overdense region in RIAF when the surface density exceeds the upper limit for RIAF. We assume that the origin of the density enhancement is the increase of the mass accretion rate from the outer region (see Figure 1(a)).

We simulate the evolution of the MHD accretion flow when the surface density of the density enhancement exceeds the upper limit for the existence of RIAF. We choose the maximum density $\rho_0 = 2 \times 10^{-11}$ g/cm³ such that the mass accretion rate of the quasi-steady nonradiative accretion flow is $0.1\dot{M}_{\text{Edd}}$ at $r = 10r_s$. Because this accretion rate exceeds the upper limit for RIAF, radiative cooling exceeds heating. Figure 5 shows the azimuthally and vertically ($|z| < 0.5r_s$) averaged radial distribution of bremsstrahlung cooling time t_{brems} and dynamical time t_{dyn} computed using

$$t_{\text{brems}} = \frac{p_{\text{gas}}/(\gamma - 1)}{\rho \kappa_{\text{ff}} a_r c T^4}, \quad (17)$$

$$t_{\text{dyn}} = r/v_\varphi, \quad (18)$$

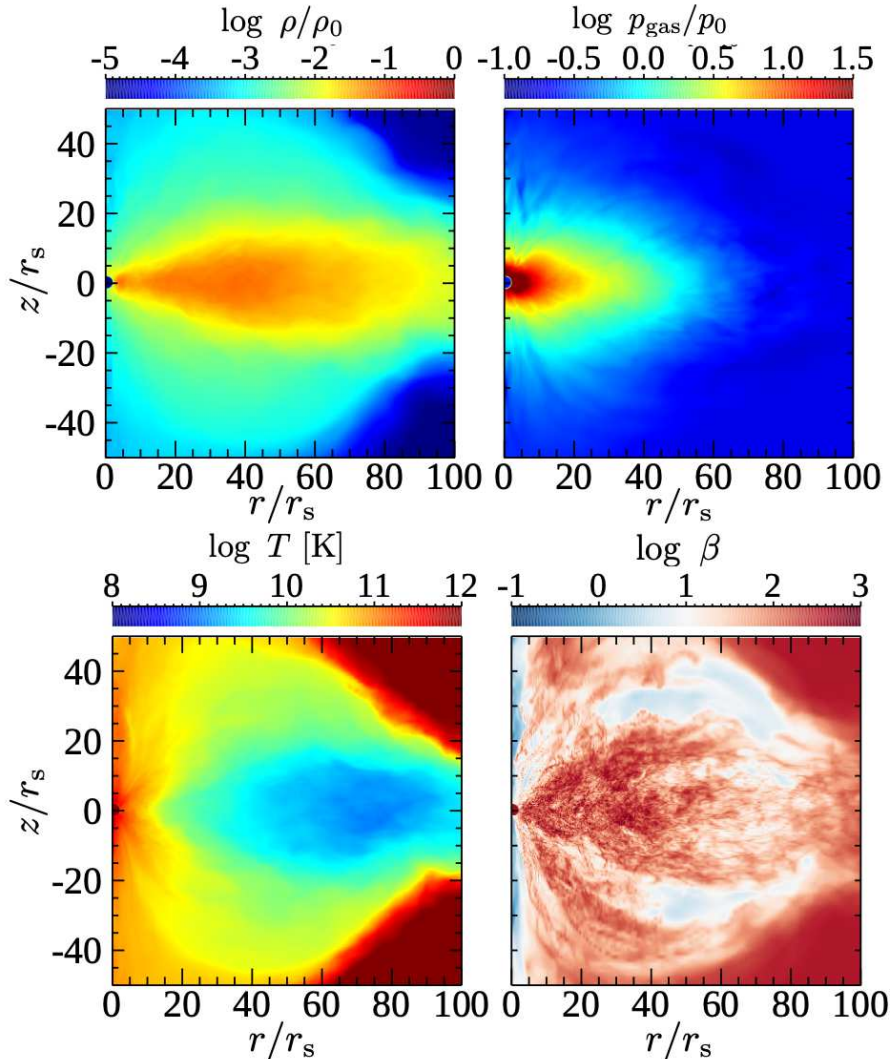


Figure 3. Azimuthally averaged distributions of density (upper left), gas pressure (upper right), gas temperature (lower left), and plasma β (lower right) in the poloidal plane at $t = t_c$.

respectively, where a_r is the radiation constant. **The cooling time scale is much longer than the dynamical time scale in the inner region ($r < 20r_s$). Meanwhile, the cooling time scale is about $10t_{\text{dyn}}$ in the outer region ($30r_s < r < 80r_s$). Because we cover more than $100t_{\text{dyn}}$ at $r = 40r_s$ in our simulation, we expect that cooling instability will grow in this region.**

3.2. Results of the radiation MHD simulation

In this section, we present the results of the RMHD simulation performed by applying the RMHD code CANS+R. In the simulation, radiation energy density E_r at $t = t_c$ is set to a negligibly small value ($E_r = 10^{-20}$ erg/cm³) in the whole region.

Figure 6 shows the distribution of gas density, gas temperature, and radiation energy density in the poloidal plane averaged over azimuthal direction and time. We pick up numerical results at three epochs. Stage 1 ($1.58 \times 10^4 t_0 < t < 1.78 \times 10^4 t_0$) is the stage just after the radiative process is included. Stage 2 ($3.05 \times 10^4 t_0 < t < 3.25 \times 10^4 t_0$) is the stage when the cool region is formed. Stage 3 ($3.90 \times 10^4 t_0 < t < 4.10 \times 10^4 t_0$) is the stage when radiation pressure becomes comparable to gas pressure. A remarkable feature of our RMHD simulation is a hybrid radial temperature

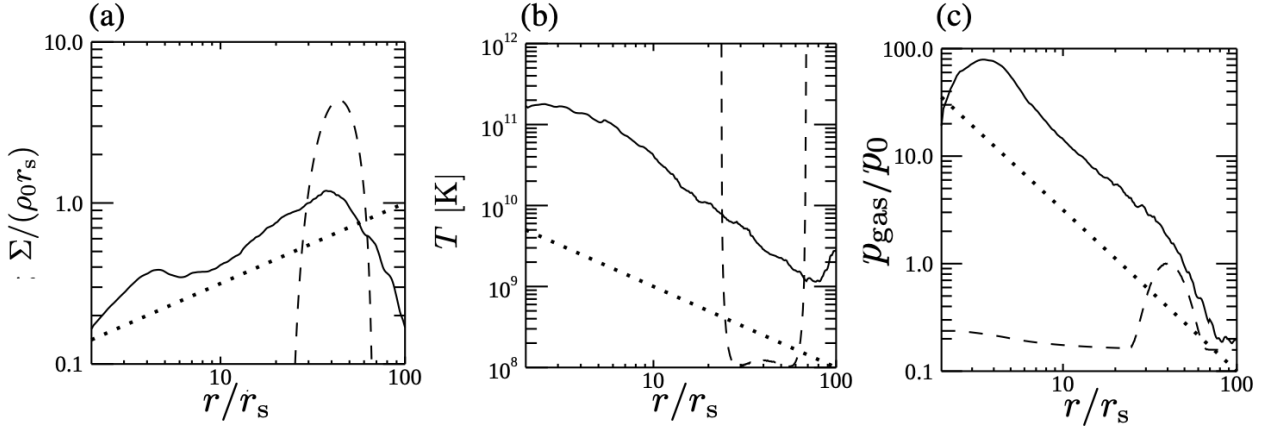


Figure 4. Azimuthally averaged radial distribution of (a) surface density, (b) gas temperature and (c) gas pressure at mid-plane ($z = 0$). Solid curves show the distribution at $t = t_c$. Dashed lines show the distribution at $t = 0$. Dotted lines show the radial dependence proportional to $r^{0.5}$, r^{-1} , and $r^{-1.5}$.

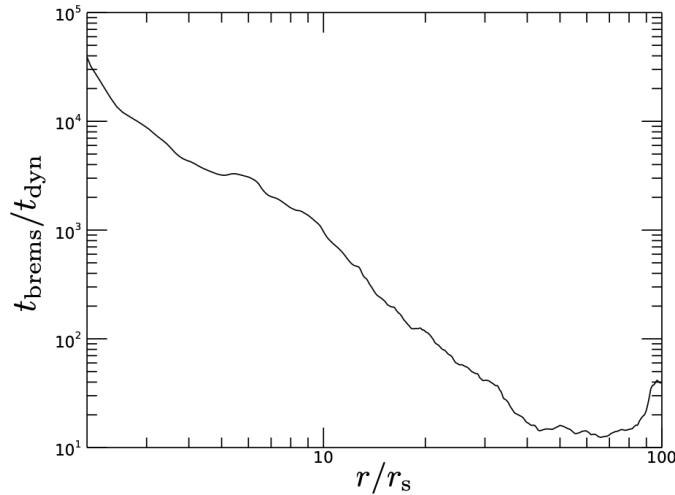


Figure 5. Azimuthally and vertically ($|z| < 0.5r_s$) averaged radial distribution of the ratio of the bremsstrahlung cooling time (t_{brems}) and dynamical time (t_{dyn}) at $t = t_c$.

distribution near the mid-plane (Figure 6(d), (e), and (f)). In the inner region ($r < 25r_s$), hot, low-density, RIAF-like accretion flow similar to those in previous nonradiative MHD simulations is sustained. In contrast, in the outer region ($r > 25r_s$), the disk shrinks in the vertical direction, and a dense and cool disk extending to $r \sim 45r_s$ appears (stage 2 and stage 3). Figure 6(e) and (f) shows that a cool region is formed by radiative cooling around the small density enhancement at $t = t_c$. The innermost region of the cool disk extends down to $r = 25r_s$. Figure 6 (b) and (c) shows

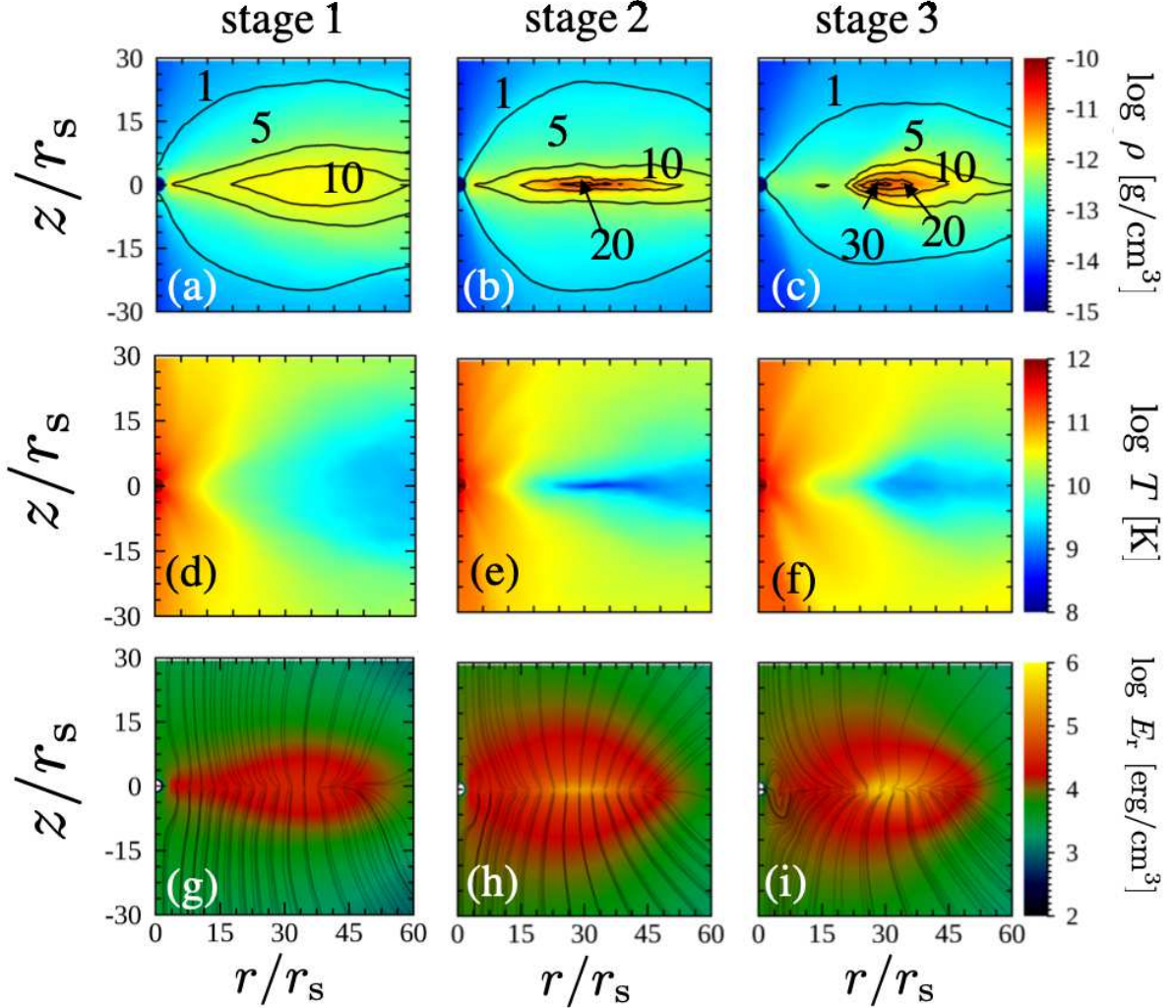


Figure 6. Azimuthally averaged gas density, gas temperature, and radiation energy density in the radiation frame. The quantities are averaged over the time range $1.58 \times 10^4 t_0 < t < 1.78 \times 10^4 t_0$ (stage 1), $3.05 \times 10^4 t_0 < t < 3.25 \times 10^4 t_0$ (stage 2) and $3.90 \times 10^4 t_0 < t < 4.10 \times 10^4 t_0$ (stage 3). Contours in (a), (b) and (c) show $\tau_{\text{es}} = 1, 5, 10, 20, 30$ and solid curves in (g), (h) and (i) show the streamlines of the radiation energy flux in the poloidal plane.

that the equatorial region of the cool disk is optically thick for Thomson scattering ($\tau_{\text{es}} \gtrsim 10$), where

$$\tau_{\text{es}} = - \int_{+50r_s}^0 \rho \kappa_{\text{es}} dz. \quad (19)$$

Thomson optical depth around the mid-plane in stage 3 becomes larger than that in stage 2 (Figure 6 (b) and (c)). Meanwhile, the disk is optically thin for absorption. The effective optical depth

$$\tau_{\text{eff}} = - \int_{+50r_s}^0 \rho \sqrt{\kappa_{\text{ff}} (\kappa_{\text{ff}} + \kappa_{\text{es}})} dz. \quad (20)$$

is $\tau_{\text{eff}} < 0.1$ in the whole region. We found that the radiation energy density increases in the cool region. Solid curves in Figure 6(g), (h), and (i) show the streamlines of radiation flux. Figure 6(h), and (i) clearly shows that most of the radiation is emitted from the cool region.

Figure 7 shows the azimuthally averaged radial distribution of gas density, surface density, gas temperature and radiation temperature, specific angular momentum, mass accretion rate and radial velocity at stage 1 (red), stage 2

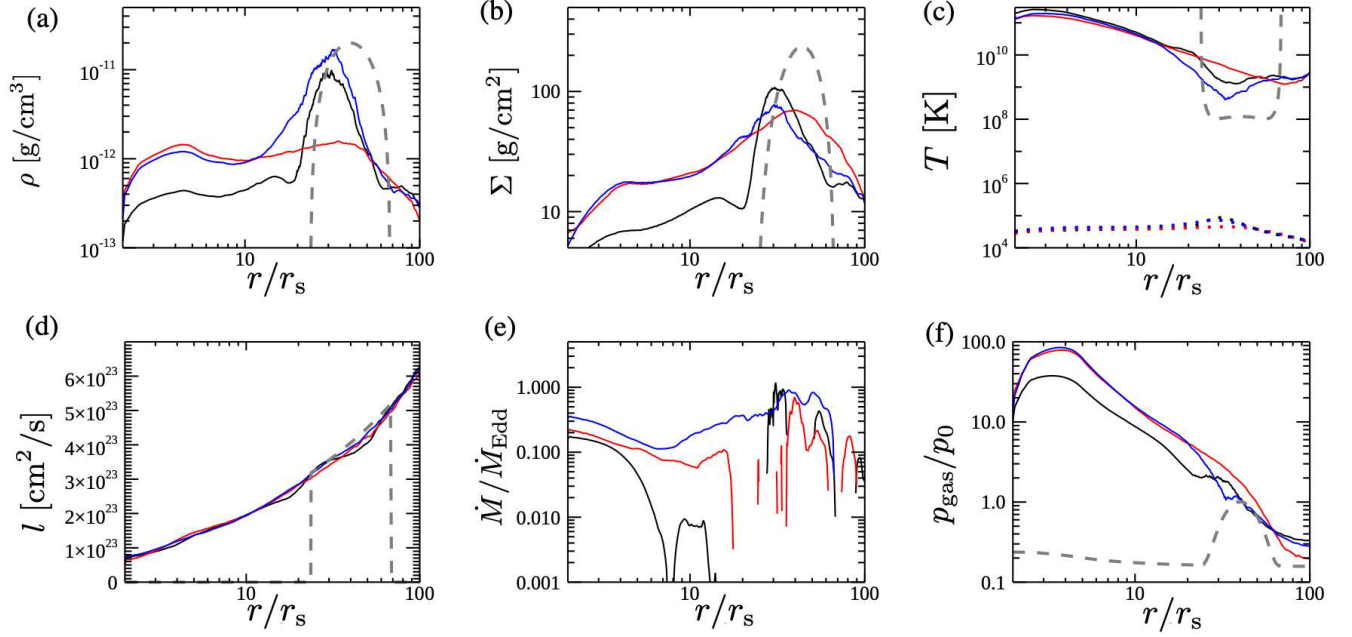


Figure 7. Time and azimuthally averaged radial distribution of (a) gas density, (b) surface density (solid), (c) gas temperature (solid) and radiation temperature (dotted), (d) specific angular momentum, (e) the mass accretion rate and (f) the gas pressure at $z = 0$. Red, blue and black curves show stage 1, stage 2 and stage 3, respectively. Dashed curves show the distribution at $t = 0$.

(blue) and stage 3 (black) at $z = 0$. Figure 7(a) shows that during the interval between stage 1 and stage 2, the density increases by a factor of 10 at $r \sim 30r_s$. In contrast, the surface density (the blue curve in Figure 7(b)) does not increase because the disk shrinks in the vertical direction. The gas temperature around $r \sim 30r_s$ increases between stage 2 and stage 3 because of the dissipation of the magnetic energy. The radiation temperature is much smaller than the gas temperature even in the cool region. Figure 7(e) shows the mass accretion rate calculated from

$$\dot{M} = - \int_0^{2\pi} \int_{-10r_s}^{10r_s} \rho v_r dz r d\varphi. \quad (21)$$

The mass accretion rate is nearly constant up to $r \sim 20r_s$ in stage 1 (the red curve) and angular momentum is close to the Keplerian distribution. Figure 7(f) shows that the radial distribution of the gas pressure is close to the CDAF solution ($p_{\text{gas}} \propto r^{-1.5}$) up to $r \sim 80r_s$ in stage 1 (red curve) and stage 2 (blue curve).

Figure 8(a) shows the three-dimensional volume rendering image of the gas temperature distribution at $t = 4.64 \times 10^4 t_0$. A cool region with a temperature of $T \sim 10^7$ K is formed locally. This temperature is lower than the azimuthally averaged temperature shown in Figure 6, and Figure 7(c) because the cool region with temperature $\sim 10^7$ K is localized. Figure 8(b) shows the space-time plot of the equatorial temperature at $\varphi = \pi$. As the cooling instability grows, a cool, soft X-ray emitting region appears in the outer disk ($r > 25r_s$). Meanwhile, the region near the black hole ($r < 25r_s$) stays hot ($T > 10^{11}$ K). Such a hybrid structure of disk temperature is also shown in general relativistic RMHD simulations (Takahashi et al. 2016). The interface between the hot region and the cool region oscillates quasi-periodically. The oscillation period is close to the Keplerian rotation period $\approx 1.0 \times 10^3 t_0$ at $r \sim 23r_s$. In the later stage ($t > 3.5 \times 10^4 t_0$), another oscillation appears in the cool outer region (see horizontal stripes in Figure 8(b)). The oscillation period is $2.0 \times 10^3 t_0$, which corresponds to the Keplerian period of the cool ($T \sim 10^{7-8}$ K) region around $r \simeq 40r_s$. A more detailed analysis of the oscillation is given in Section 3.3.

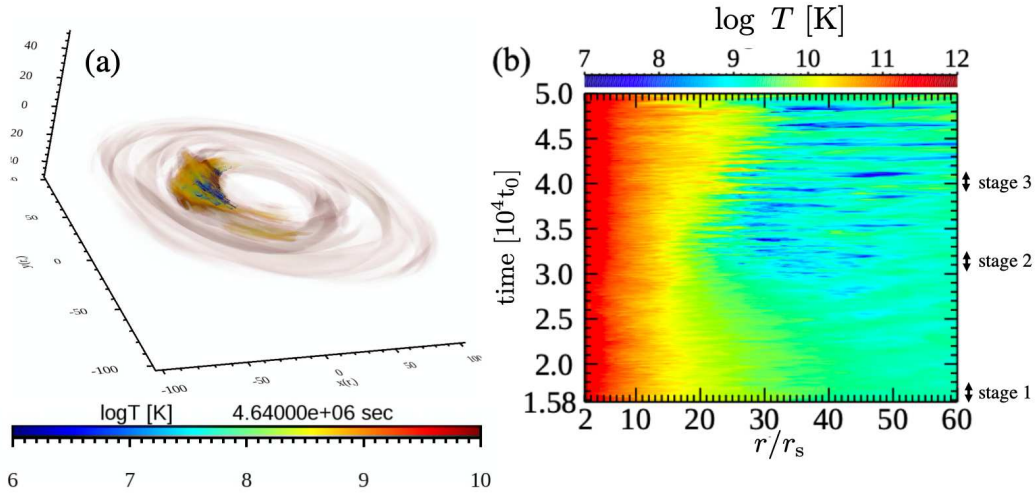


Figure 8. (a) Three-dimensional volume rendering image of gas temperature distribution at $t = 4.64 \times 10^4 t_0$. (b) The space-time diagram of gas temperature on the equatorial plane at $\varphi = \pi$.

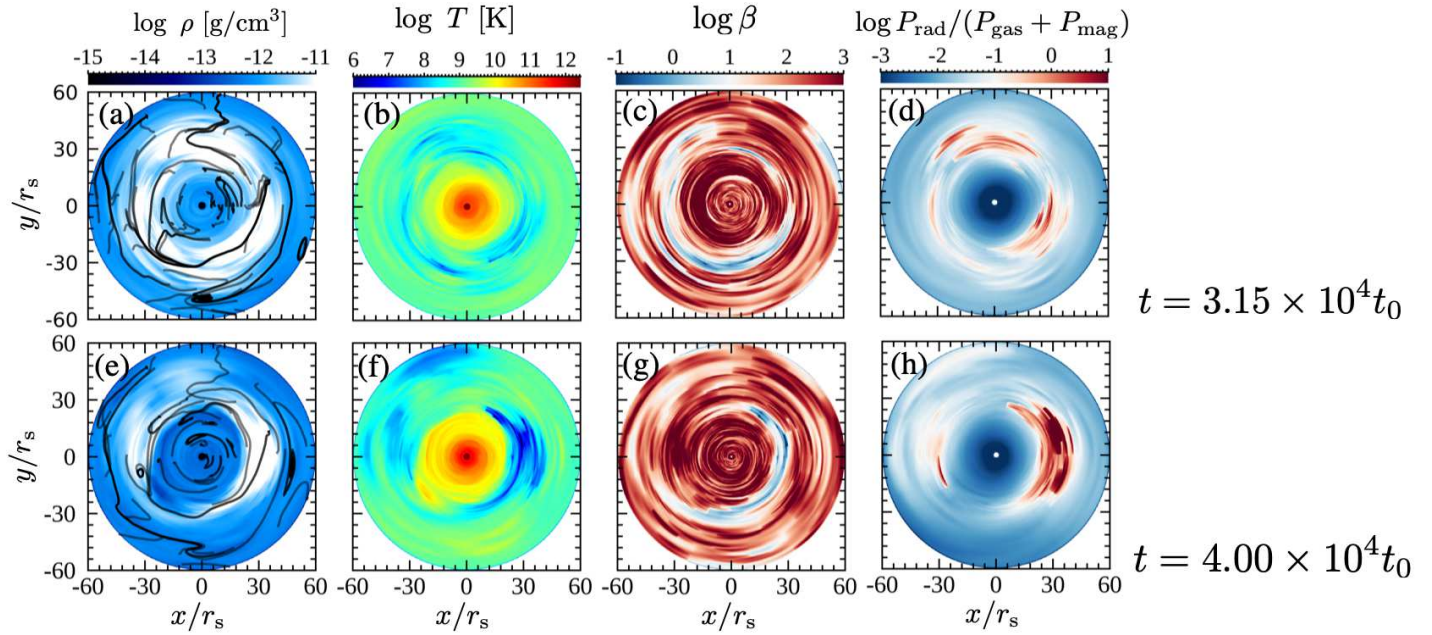


Figure 9. Snapshots of the density, gas temperature, plasma β and $p_{\text{rad}} / (p_{\text{gas}} + p_{\text{mag}})$ in the xy plane averaged in $|z| < 0.5 r_s$. The upper panels show the quantities at $t = 3.15 \times 10^4 t_0$ and the lower panels show that at $t = 4.00 \times 10^4 t_0$. Solid curves in panels (a) and (e) show magnetic field lines.

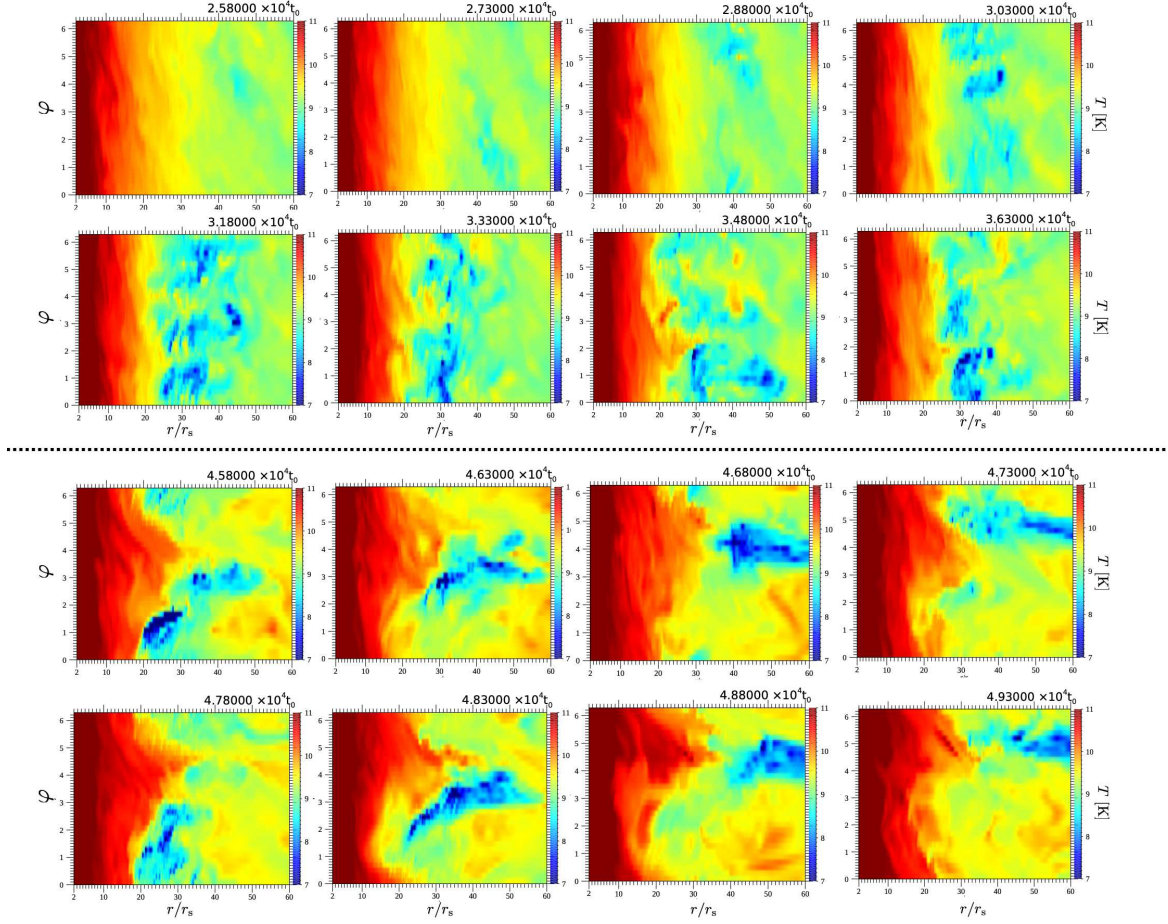


Figure 10. The time evolution of the gas temperature distribution in $r - \varphi$ plane averaged in $|z| < 0.5r_s$. The upper eight panels show the onset of the cooling instability and the lower eight panels show the later stage.

Figure 9 shows snapshots of the density, gas temperature, plasma β and $p_{\text{rad}}/(p_{\text{gas}} + p_{\text{mag}})$ in the xy plane averaged in $|z| < 0.5r_s$. Figure 9(a), (b) and (c) shows that a dense, low- β and cool, soft X-ray emitting region appears outside the inner hot flow ($r > 25r_s$) at $t = 3.15 \times 10^4 t_0$. The dense, cool region has a nonaxisymmetric distribution. Asymmetry becomes more prominent at $t = 4.00 \times 10^4 t_0$. Furthermore, Figure 9(h) shows that the radiation pressure becomes dominant in the cool region. The effective optical depth of this region is less than unity but radiation is trapped because the Thomson optical depth is large. The solid curves in Figure 9(a) and (e) show magnetic field lines projected onto the xy plane. The magnetic fields are nearly azimuthal in Figure 9(a) but deformed into a spiral shape in Figure 9(e).

Figure 10 shows the time evolution of the gas temperature distribution in the $r - \varphi$ plane averaged in $|z| < 0.5r_s$. Panels above the dotted line show the onset of the cooling instability. Between $t = 2.58 \times 10^4 t_0$ and $t = 2.88 \times 10^4 t_0$, the temperature gradually decreases from $10^{9.5}$ K to $10^{8.5}$ K around $r \sim 45r_s$. The temperature distribution has weak nonaxisymmetry. A cool blob with temperature $T = 10^7$ K is formed around $t = 3.03 \times 10^4 t_0$. This cool blob rotates along nearly circular orbit with the local Keplerian rotation speed. The lower panels in Figure 10 show the temperature distribution in the later stage with a shorter time interval. The cool region oscillates radially between $r = 20r_s$ and $60r_s$ with a period around $2.0 \times 10^3 t_0$. The cool region is not axisymmetric but localized within a finite azimuthal angle. In addition, a one-armed pattern grows around the interface between the hot flow and cool disk, and rotates slowly in the azimuthal direction.

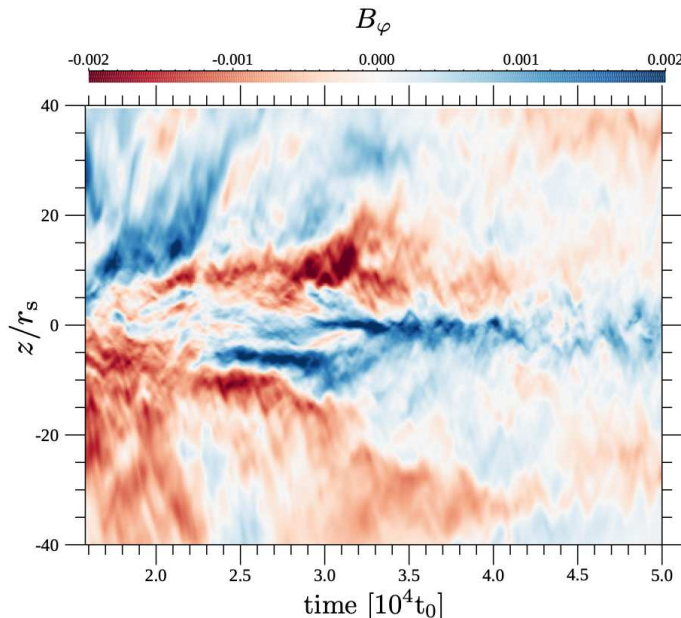


Figure 11. Butterfly diagram of azimuthally averaged azimuthal magnetic fields averaged in the radial range $25r_s < r < 35r_s$.

Figure 11 shows the butterfly diagram of the azimuthal magnetic field. The horizontal axis is time, and the vertical axis is height. The color shows the azimuthal magnetic field averaged in $25r_s < r < 35r_s$. The azimuthal magnetic fields buoyantly escape from the disk to the disk corona. The azimuthal magnetic field at mid-plane increases because of the vertical contraction of the disk. Because the azimuthal magnetic fields are antisymmetric with respect to the disk mid-plane, they dissipate by magnetic reconnection. This can be the origin of the heating observed in Figure 7(c). The azimuthal magnetic field occasionally changes its sign and buoyantly escapes from the disk.

Figure 12 shows the time evolution of the α parameter (Shakura & Sunyaev 1973), calculated by,

$$\alpha = -\frac{\langle B_r B_\varphi \rangle}{\langle p_{\text{gas}} + p_{\text{rad}} \rangle} \quad (22)$$

where $\langle \rangle$ denotes the volume-weighted average in the cylindrical coordinate and blue, orange, and red show α computed by averaging the region $2r_s < r < 20r_s$, $20r_s < r < 25r_s$, and $25r_s < r < 50r_s$, with $|z| < 5r_s$. In the inner region (blue curve), $\alpha \sim 0.02$ is sustained until $t \sim 2.5 \times 10^4 t_0$, when the magnetic flux buoyantly escapes from the disk. In the outer region (orange and red curve), α increases during the contraction of the disk in $2.7 \times 10^4 t_0 < t < 3.3 \times 10^4 t_0$ because the azimuthal magnetic field is enhanced in the mid-plane because of vertical contraction. In the later stage ($t > 4.5 \times 10^4 t_0$), α increases again in the inner region because magnetic fields are regenerated by the dynamo activity. The mass accretion is sustained in the whole disk because of the angular momentum transport driven by the Maxwell stress.

Figure 13 shows the scatter plot of Σ and \dot{M} at various sampling radii. Dashed curves are thermal equilibrium curves of RIAF at $r = 5r_s$ (blue) and $r = 30r_s$ (red) when the viscosity parameter is $\alpha = 0.01$. The dash-dotted line shows the relation $\dot{M} \propto \Sigma$. Numerical results in the hot inner region ($r < 25r_s$: blue, green, and purple) follow RIAF solutions of $\dot{M} \propto \Sigma$. Note that the accretion rate becomes smaller near the black hole because of the outflows from the hot region. In contrast, numerical solutions in the cool outer region ($r > 25r_s$: orange and red) scatter along with the extension of the RIAF solution, and the oscillations occur when the electron scattering optical depth becomes larger than ~ 10 . Steady solutions of black hole accretion flow connecting the optically thin RIAF and optically thick standard disk have been obtained by Oda et al. (2009) considering the azimuthal magnetic fields. In their solution, radiative cooling is balanced with heating by the dissipation of magnetic energy enhanced by the vertical contraction of the disk because of cooling. Furthermore, the disk stays geometrically thicker than the standard model because

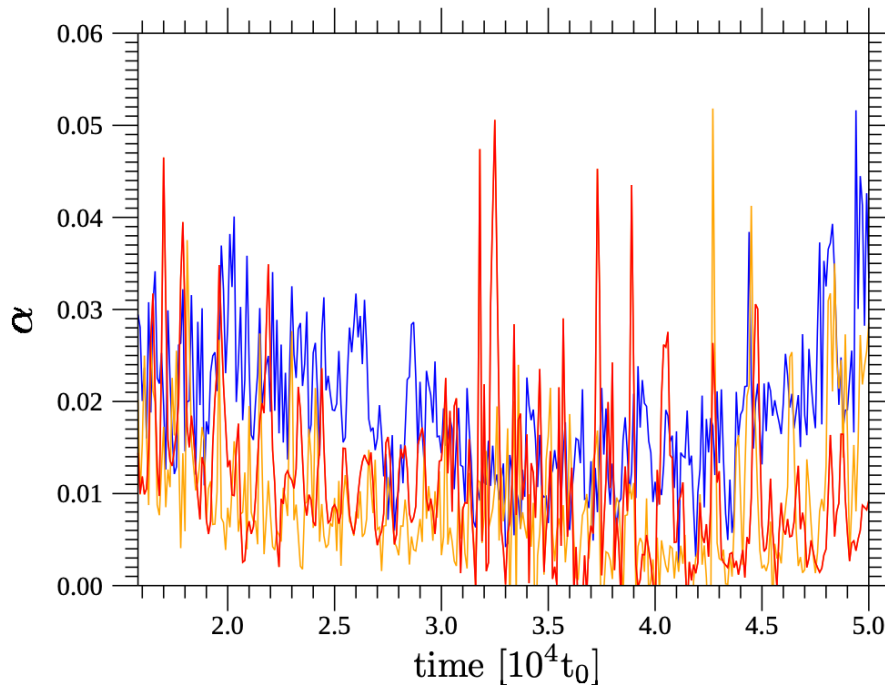


Figure 12. Time evolution of $\alpha = - \langle B_r B_\varphi \rangle / \langle p_{\text{gas}} + p_{\text{rad}} \rangle$ averaged over $2r_s < r < 20r_s$ (blue), $20r_s < r < 25r_s$ (orange), and $25r_s < r < 50r_s$ (red), with $|z| < 5r_s$

the magnetic pressure gradient can support the disk (see also Jiang et al. 2019a). We should note, however, that the solutions by Oda et al. (2009) are for stellar-mass black holes. When the mass of the black hole is $10^7 M_\odot$, radiation pressure is not negligible when the accretion rate exceeds 1% of the Eddington accretion rate.

3.3. Quasi-periodic oscillations excited during the formation of the soft X-ray emitting region

One of the most remarkable findings is that the disk oscillates quasi-periodically as the soft X-ray emitting region is formed outside the inner hot RIAF. Figure 14 (a) shows the space–time diagram of the azimuthally averaged radial velocity in $|z| < 0.5r_s$. The radial oscillation becomes prominent around $r \sim 23r_s$ in $3.05 \times 10^4 t_0 < t < 3.25 \times 10^4 t_0$ (stage 2) when the interface between the hot inner RIAF and the cool outer region settles around this radius. The oscillation period is $2\pi/\omega_0 = 1.0 \times 10^3 t_0$, which is close to the Keplerian rotation period at $r = r_{c0} \sim 23r_s$. It should be noted that azimuthally averaged radial velocity is positive around this radius. This indicates that the infalling cool blobs are overreflected as shown in the bottom panels of Figure 10.

Another oscillation appears around $r \sim 40r_s$ where the cooling instability grows. This oscillation can be excited by the vertical contraction of the disk because of radiative cooling. The vertical contraction induces flattening of the disk as shown in Figure 6(e). Subsequently, the disk thickens (see Figure 6(f)), and oscillates mainly in the radial direction. The amplitude of this oscillation grows with time and becomes prominent when $t > 3.5 \times 10^4 t_0$. The period of the large-amplitude oscillation is $\sim 2.0 \times 10^3 t_0$. This period is close to the Keplerian rotation period at $r \sim 40r_s$. This oscillation is nonaxisymmetric radial pulsation with an azimuthal mode number $m = 1$ as shown in Figure 10.

The black curve in Figure 14(b) shows the time variation of the disk bolometric luminosity L_z measured at $z = 30r_s$, computed by

$$L_z = \int_0^{2\pi} \int_{r_{\text{in}}}^{r_{\text{out}}} F_z(z = 30r_s) dr r d\varphi, \quad (23)$$

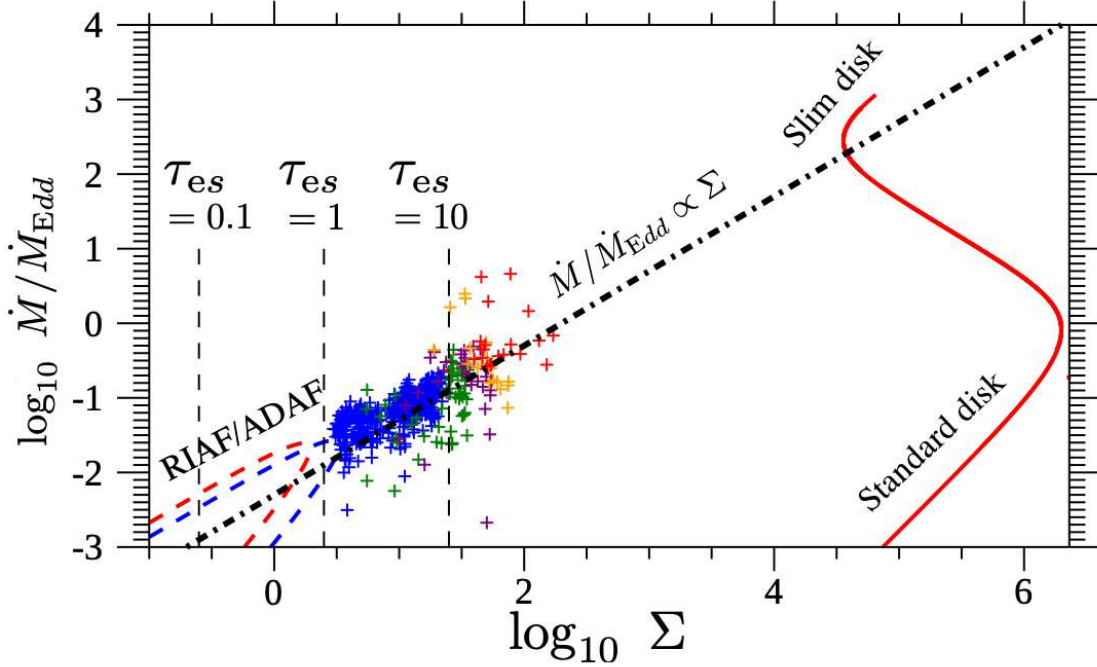


Figure 13. Scatter plot of the surface density and mass accretion rate at the sampling radii $r = 5r_s$ (blue), $15r_s$ (green), $20r_s$ (purple), $25r_s$ (orange), and $30r_s$ (red) and averaged over the Keplerian rotation period at each radius. The dashed blue curve and dashed red curve show equilibrium solutions of optically thin RIAF at $r = 5r_s$ and $r = 30r_s$, and a solid red curve shows an optically thick solution at $r = 30r_s$ for $\alpha = 0.01$ and $M_{\text{BH}} = 10^7 M_{\odot}$.

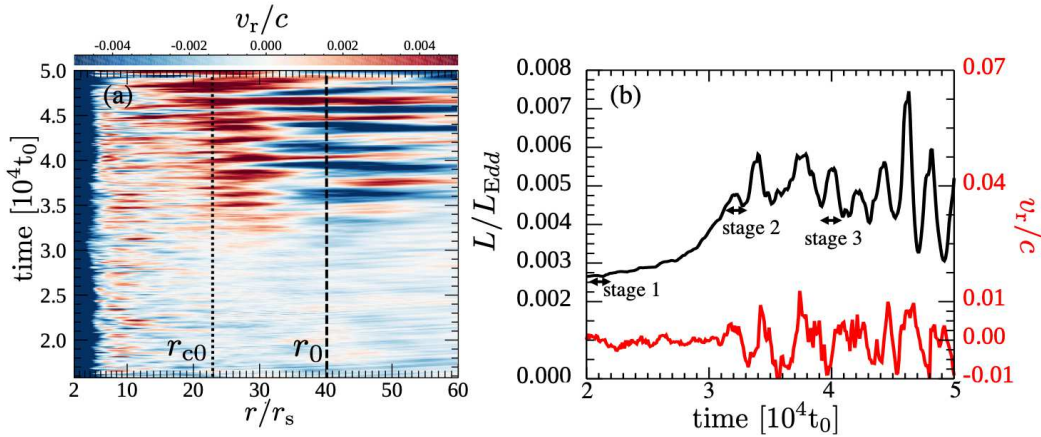


Figure 14. (a) Space-time diagram of the radial velocity averaged in the azimuthal direction and $|z| < 0.5r_s$. (b) Disk bolometric luminosity (black) and radial velocity at $z = 0$ averaged over $0 < \varphi < 2\pi$ in $42r_s < r < 44r_s$ (red). The dotted line in (a) indicates the corotation radius r_{c0} , where the oscillation period equals $1.0 \times 10^3 t_0$. The dashed line in (a) indicates the radius of the initial density maximum at $r = r_0$.

where $r_{\text{in}} = 0$ and $r_{\text{out}} = 200r_s$. Between stage 1 and stage 2, the disk luminosity gradually increases up to roughly 0.5% of the Eddington luminosity. Later, it starts to oscillate quasi-periodically, and the amplitude of the oscillation gradually increases. The short time scale variabilities observed in the rising stage of CLAGN (Noda et al. 2016) can be generated by this oscillation. The oscillation period

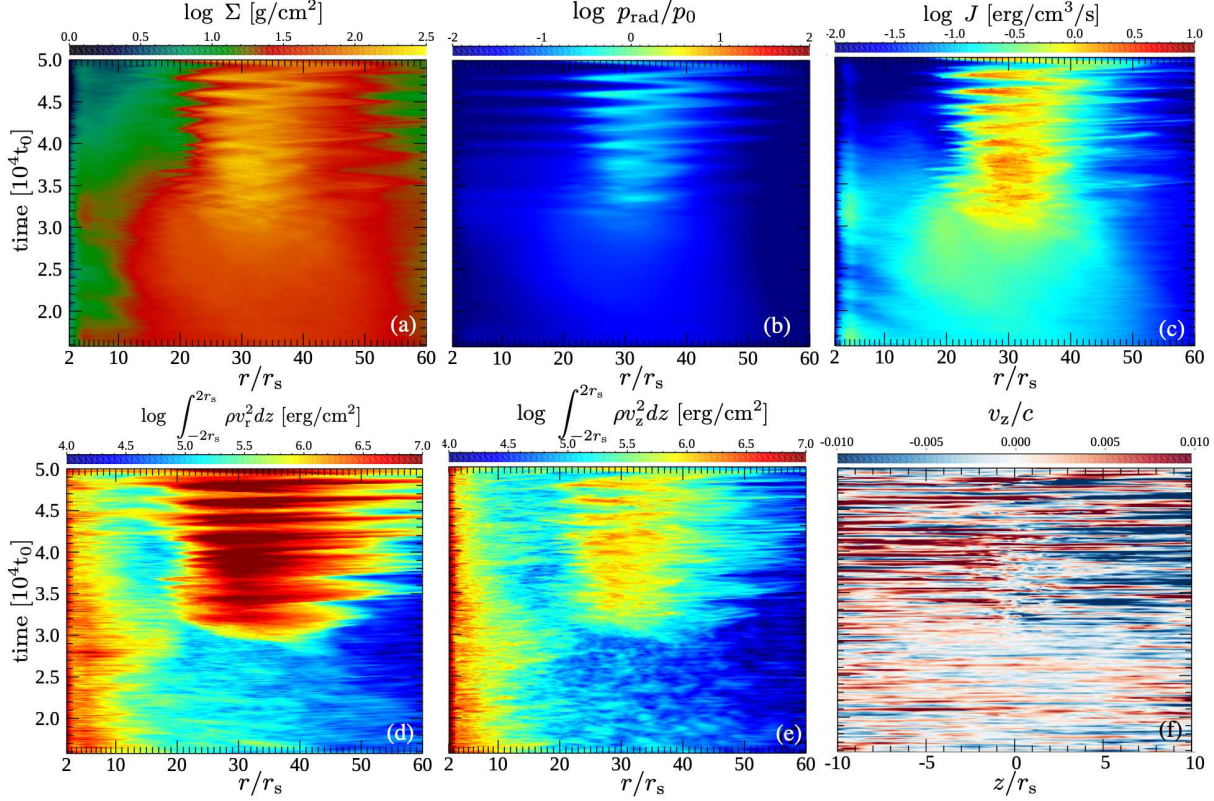


Figure 15. Space–time diagram of the azimuthally averaged (a) surface density, (b) radiation pressure, and (c) net emissivity J in the r –time plane. The radiation pressure and emissivity are averaged in $|z| < 0.5r_s$. (e) and (f) are space–time diagrams of the kinetic energy density in radial and vertical motion integrated in $|z| < 2r_s$. (f) shows a space–time diagram of the azimuthally averaged vertical velocity at $r = 30r_s$ in the z –time plane.

of the disk luminosity is close to the oscillation period of the large-amplitude radial pulsation. The red curve in Figure 14(b) shows the time variation of the radial velocity averaged over the azimuthal direction in $42r_s < r < 44r_s$. The time variation of the radial velocity is almost coherent with the luminosity in $3.0 \times 10^4 t_0 < t < 3.8 \times 10^4 t_0$ but anticorrelates when $t > 3.8 \times 10^4 t_0$ because the luminosity peak coincides with time when the cool blob begins to move outward (see Figure 10 at $t = 4.58 \times 10^4 t_0$ and $t = 4.78 \times 10^4 t_0$).

Figure 15 shows the space–time diagram of azimuthally averaged quantities. Figure 15(a) shows the time variability of the surface density. Figure 15(b) and (c) shows the space–time diagrams of the radiation pressure, and net emissivity $J = \rho \kappa_{\text{ff}} c (a_r T_{\text{gas}}^4 - E_r)$ averaged in $|z| < 0.5r_s$, respectively (see Figure 8(b) for temperature). We take the azimuthal average to focus on the radial oscillation. The physical quantities oscillate almost coherently in $20r_s < r < 40r_s$. Figure 15(d) and (e) shows the time variation of the azimuthally averaged kinetic energy in radial and vertical motion integrated in $|z| < 2r_s$. After the cool region is formed, both the radial and vertical kinetic energy increase. Figure 15(f) shows the time variation of the vertical velocity in z –time plane. Between $t = 3.0 \times 10^4 t_0$ and $t = 4.0 \times 10^4 t_0$, the vertical velocity becomes antisymmetric to the mid-plane. This antisymmetry is produced due to the vertical contraction by the cooling instability.

Figure 16 shows the power spectral density (PSD) of the azimuthally averaged radial velocity at the mid-plane. The PSDs are computed by Fourier transformation of the time evolution of the azimuthally averaged radial velocity at each radius. Panels (a), (b), and (c) show the PSD in the time interval $1.58 \times 10^4 t_0 < t < 3.0 \times 10^4 t_0$, $3.05 \times 10^4 t_0 < t < 3.9 \times 10^4 t_0$, and $3.9 \times 10^4 t_0 < t < 5.0 \times 10^4 t_0$, respectively. The

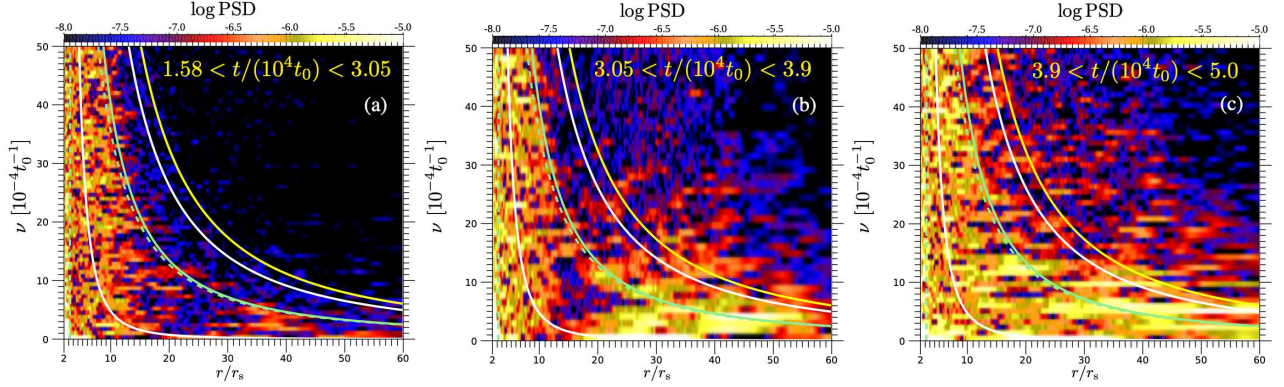


Figure 16. The power spectral density (PSD) of the azimuthally averaged radial velocity at mid-plane. The vertical axis is frequency and horizontal axis is radius. (a), (b), and (c) show the PSD in the time interval in $1.58 \times 10^4 t_0 < t < 3.05 \times 10^4 t_0$, $3.05 \times 10^4 t_0 < t < 3.9 \times 10^4 t_0$, and $3.9 \times 10^4 t_0 < t < 5.0 \times 10^4 t_0$, respectively. Green solid and dashed curves are the Keplerian rotation frequency $\Omega_K/(2\pi)$ and $\kappa/(2\pi)$ where κ is the epicyclic frequency. White solid curves show $(\Omega_K \pm \kappa)/(2\pi)$, and the yellow curve shows $(1 + \sqrt{2})\Omega_K/(2\pi)$.

green solid and dashed curves show the Keplerian rotation frequency $\Omega_K/(2\pi)$ and $\kappa/(2\pi)$, respectively, where κ is the epicyclic frequency. The white solid curves show $(\Omega_K \pm \kappa)/2\pi$ and the yellow solid curves show $(1 + \sqrt{2})\Omega_K/(2\pi)$. The PSD can be explained by applying the theory of disk oscillation (e.g., Kato 2016). The local dispersion relation for accretion disks is summarized by Kato (2001) as

$$\{(\omega - m\Omega_K)^2 - \kappa^2\}\{(\omega - m\Omega_K)^2 - n\Omega_K^2\} = k_r^2 c_s^2 (\omega - m\Omega_K)^2, \quad (24)$$

where ω is the wave angular frequency, n is the mode number in the vertical direction, k_r is the radial wave number, and c_s is the sound speed. This dispersion relation is derived by assuming that the disk is isothermal in the vertical direction near the equatorial plane. When $n = 0$, waves can propagate in the region satisfying $|\omega - m\Omega_K| > \kappa$. These are p-mode waves. When $n \neq 0$, because $\kappa < \Omega_K$, waves can propagate in the region satisfying $-\kappa < \omega - m\Omega_K < \kappa$ (g-mode) or $|\omega - m\Omega_K| > \sqrt{n}\Omega_K$ (c-mode when $n = 1$ and vertical p-mode otherwise).

In the early stage (Figure 16(a)), oscillations with frequency $\nu > 1.0 \times 10^{-3} t_0^{-1}$ are localized in the hot region ($r < 23r_s$), and the oscillation frequency is less than the epicyclic frequency. Figure 16(b) shows the stage when the disk shrinks in the vertical direction because of cooling. As Figure 15(f) shows, the $n = 2$ mode, in which v_z is antisymmetric to the equatorial plane is excited. The propagation region of the $m = 1$ and $n = 2$ g-mode wave is $\Omega_K - \kappa < \omega < \Omega_K + \kappa$ (white curves in Figure 16). The low-frequency oscillation with frequency $\nu = 4.0 \times 10^{-4} t_0^{-1}$ is consistent with this theory. Another oscillations appear along $\omega = \kappa$. These are oscillations with local epicyclic frequency. High-frequency oscillations with frequency above Ω_K are p-mode waves. Figure 16(c) shows the later stage when larger amplitude radial oscillation dominates.

Let us discuss the origin of the large-amplitude radial oscillation. There can be two mechanisms to amplify the oscillation. One is the pulsational instability in which the radial oscillation becomes overstable (e.g., Kato 1978; Blumenthal et al. 1984). The other is the corotation instability in which radially propagating p-mode waves are overreflected at the corotation point (e.g., Drury 1985; Kato 1987; Tsang & Lai 2009). In Figure 16(b) oscillation with frequency $\nu \sim 1.0 \times 10^{-3} t_0^{-1}$ appears around $r = 23r_s$. Because $r = r_{c0} \sim 23r_s$ is the corotation radius of the $m = 1$ wave with angular frequency

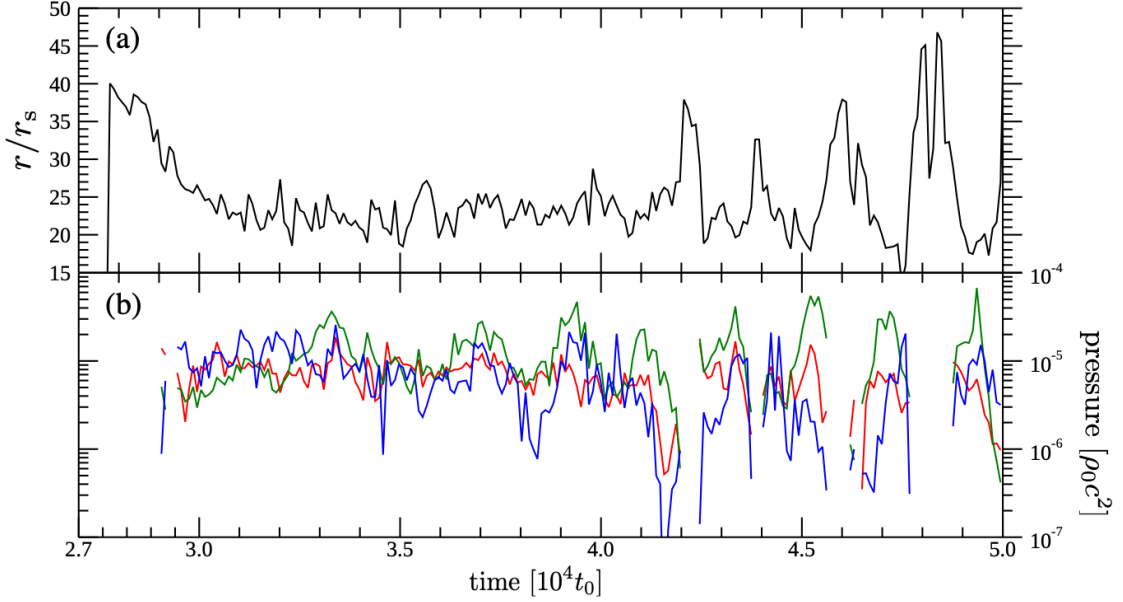


Figure 17. Time variation of the (a) innermost radius of the cool region where $T < 5 \times 10^7$ K at the mid-plane, (b) p_{gas} (red), p_{mag} (blue), and p_{rad} (green) averaged in the cool region ($T < 5 \times 10^7$ K) inside $r = 30r_s$

$\omega_0 = \Omega_K(r_{c0})$, a corotation resonance can be responsible for the oscillation at $\omega = \omega_0$ localized around $r = r_{c0}$ in Figure 16(b) and (c).

It should be noted that g-mode waves are not overreflected at the corotation point (Kato 2016). Because the low-frequency oscillations below Ω_K in Figure 16 are most likely g-mode waves, they are not amplified by the corotation instability at this frequency. The low-frequency oscillations with frequency $\nu = 5.0 \times 10^{-4} t_0^{-1}$ in Figure 16(c) correspond to the large-amplitude radial oscillation of the cool region around $r = r_0 \sim 40r_s$ (see Figure 10, Figure 14 and 15). Figure 17(a) shows the time variation of the innermost radius of the cool region where $T < 5 \times 10^7$ K at the mid-plane. The cool region appears around $t \sim 2.7 \times 10^4 t_0$ at $r \sim 40r_s$ and the interface between the hot and cool region moves toward $r \sim 20r_s$. The radius of the interface is almost constant until $t \sim 3.6 \times 10^4 t_0$ but oscillates after this stage. The amplitude of the displacement of the radius of the cool region increases with time. Figure 17(b) shows p_{gas} (red), p_{mag} (blue), and p_{rad} (green) averaged in the cool region ($T < 5 \times 10^7$ K) inside $r = 30r_s$. The amplitude of the radial pulsation is small until the radiation pressure exceeds the gas pressure and the magnetic pressure. Since the growth rate of the radial pulsational instability in radiation pressure dominant disk is larger than that in gas pressure dominant disk (e.g., Blumenthal et al. 1984), the pulsational instability can be the origin of the amplification of the radial pulsation.

For nonaxisymmetric perturbations, Wu et al. (1995) showed that the growth rate of the nonaxisymmetric radial oscillation increases with the azimuthal mode number in radiation pressure dominant disks. There is a possibility, however, that strong azimuthal magnetic fields suppress the growth of the nonaxisymmetric radial pulsation. The effects of the azimuthal magnetic fields on the radial pulsation has been studied by several authors (e.g., Yang et al. 1995) but their analysis is limited to axisymmetric perturbations. When the growth of the nonaxisymmetric pulsational instability is suppressed by strong azimuthal magnetic fields, the amplification of the radial pulsation will only be possible when the radiation pressure exceeds the gas pressure and the magnetic pressure.

4. SUMMARY AND DISCUSSION

In this paper, we presented the results of a global three-dimensional RMHD simulation of AGN accretion flow when $\dot{M} \sim 0.1\dot{M}_{\text{Edd}}$ and our results are as follows;

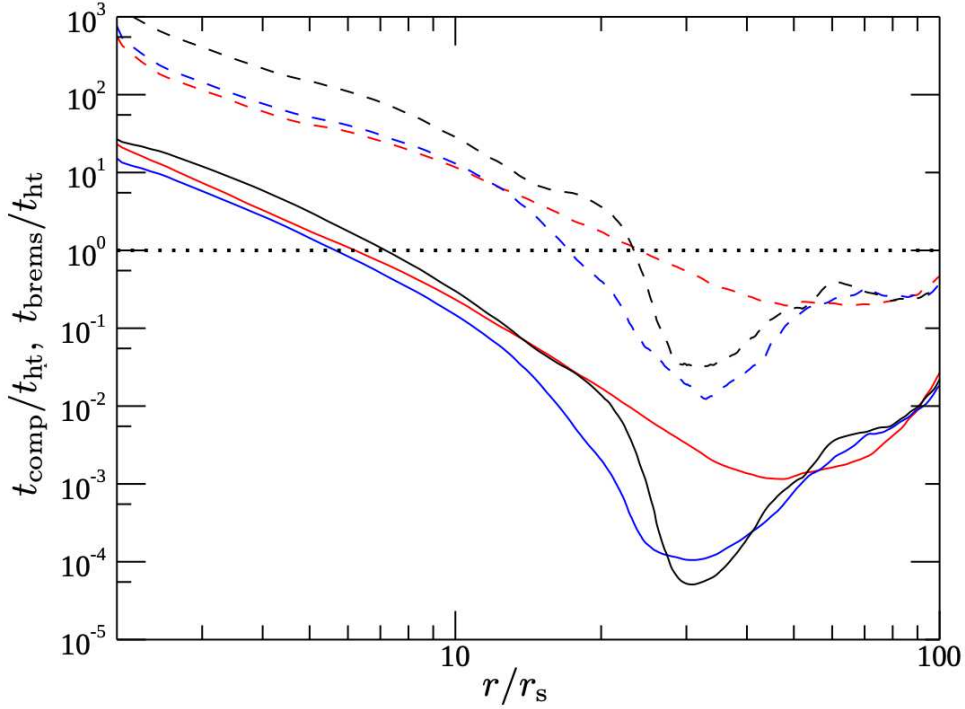


Figure 18. The azimuthally averaged radial distribution of the ratio of bremsstrahlung cooling time to viscous heating time (dashed curve) and the Compton cooling time to viscous heating time (solid curve) averaged in $|z| < 0.5r_s$. Red, blue and black curves show stage 1, stage 2 and stage 3, respectively. The dotted horizontal line shows the value of unity.

- The soft X-ray emitting, cool ($T \sim 10^{7-8}$ K) and dense region forms outside the inner RIAF by radiative cooling.
- Radiation pressure becomes dominant in the cool region.
- The region has a nonaxisymmetric structure with azimuthal mode number $m = 1$.
- The region shows quasi-periodic oscillation.

4.1. Effects of Compton scattering

X-ray observations of Seyfert galaxies indicate that soft X-ray excess component is emitted from the region with electron temperature $T_e = 10^{6-7}$ K and Thomson optical depth $\tau_{es} \sim 10$ (e.g., Done et al. 2012; Petrucci et al. 2018). These are consistent with the results of our simulations.

In the RMHD simulation we reported in this paper, inverse Compton scattering is not included. Inverse Compton scattering of soft photons by hot electrons in RIAF produces hard X-rays. Because the radiation temperature is smaller than the gas temperature except for the mid-plane of the cool region, electrons can be cooled by inverse Compton scattering. **Figure 18 shows the radial distribution of the ratio of bremsstrahlung cooling time (t_{brems}) to heating time (t_{ht}) and the Compton cooling time (t_{comp}) to heating time, where t_{comp} and t_{ht} are calculated from**

$$t_{comp} = \frac{p_{gas}/(\gamma - 1)}{\left(\rho \kappa_{es} c E_{r0} \frac{4k_B(T_e - T_r)}{m_e c^2}\right)}, \quad (25)$$

where T_r is the radiation temperature and

$$t_{ht} = t_{dyn}/\alpha. \quad (26)$$

Here we assume that the electron temperature is $T_e = \min(10^9 \text{ K}, T)$, and $\alpha = 0.015$.

Figure 18 shows that the time scale of Compton cooling is longer than the viscous heating timescale (= advection time scale) in the hot region where $r < 10r_s$. Therefore, the hot accretion flow will stay hot even when we include the inverse Compton scattering. This result is consistent with the result of the GRMHD simulation by Takahashi et al. (2016). Because the cooling time by inverse Compton scattering becomes shorter than the heating time scale in the region $r > 10r_s$, the region will shrink in the vertical direction faster than our simulation without Compton cooling. The radius of the interface between the hot inner region and the cool outer region could move inward when inverse Compton scattering is considered. However, the quasi-steady state of the cool disk will not change even when we consider Compton cooling because the Compton cooling time becomes longer as the electron temperature decreases. We should note that the Compton cooling time shown in Figure 18 is computed using the azimuthally averaged temperature. As we showed in Figure 9 (f), the electron temperature can be as low as 10^7 K. Because the Compton cooling time is proportional to $1/(T_e - T_r)$, it becomes 100 times longer in this region, and becomes comparable to the bremsstrahlung cooling time. We expect that the gas temperature stays at 10^{6-7} K by balancing the dissipative heating and radiative cooling (e.g., Oda et al. 2009, 2012). The inverse Compton scattering also cools the ambient gases above the disk mid-plane where the Thomson optical depth is larger than 1 (see Figure 6). When the electron temperature is 10^9 K and $\tau_{es} = 1$, the Compton y -parameter is larger than 0.8 so that the inverse Compton scattering is not negligible. The region will shrink in the vertical direction until the disk is supported by the sum of gas pressure, radiation pressure, and magnetic pressure.

4.2. Oscillation of the radiation-pressure-dominant region

The numerical results indicate that a large-amplitude oscillation is excited when the radiation pressure of the cool region exceeds the magnetic pressure and gas pressure. Such region appears when the luminosity exceeds 0.5% of the Eddington luminosity. The total luminosity of the accretion flow oscillates in coherence with the large-amplitude radial pulsation. The typical frequency of the large-amplitude pulsation coincides with the Keplerian angular frequency of the dense, cool region. When the mass of the black hole is $10^7 M_\odot$, the typical period of the oscillation is 2.0×10^5 s.

We should note that the luminosity variation is not because of the rotation of the dense, cool blob because the luminosity is computed by integrating the radiative flux emitted from the disk in $0 < r < 200r_s$. Therefore, the contribution from the nonaxisymmetric distribution is averaged out. We suggest that the rapid X-ray time variabilities observed during the changing-look phenomena (e.g., Noda et al. 2014) can be because of this oscillation. Recently, Jin et al. (2020) reported that QPO with period 3.58×10^3 s is observed in the narrow line Seyfert 1 galaxy RE J1034+396 whose black hole mass is $\sim 2 \times 10^6 M_\odot$. This period is shorter than that in our simulations. We speculate that the oscillation is excited in regions closer to the central black hole.

Let us discuss the dependence on the initial density distribution. If the radial pulsation is amplified when the radiation pressure becomes significant, the oscillation period is determined by the Keplerian rotation period of the radiation-pressure-dominant region. When the accretion rate is 1 – 10% of the Eddington accretion rate, the radius of the radiation-pressure-dominant region is less than $100r_s$. Therefore, the oscillation frequency is not so different from our simulations. When the accretion rate is higher, the oscillation period can be longer because the size of the radiation-pressure-dominant region becomes larger. In such disks, however, thermal instability can collapse the disk to geometrically thin, standard disks as shown by Mishra et al. (2016). The quasi-periodic oscillations may occur only when the accretion rate is 1 – 10% of the Eddington accretion rate, so that the radiation-pressure-dominant region is limited to $r < 100r_s$.

Considering the above discussions, we need to carry out simulations with different initial density profiles to confirm that the QPOs are excited not at the radius of the initial dense blob but in the region where radiation pressure exceeds the gas pressure and magnetic pressure.

4.3. Final remarks

In the simulation presented in this paper, we only used 32 grid points in the azimuthal direction. Matsumoto et al. (2019) showed that the saturation value of the α is almost independent of the resolution, but the

time scale for the saturation becomes shorter in high-resolution simulations. They also showed that to resolve the growth of MRI, we need at least 128 grid points in the azimuthal direction. However our essential results do not change even if the azimuthal modes are resolved or if the accretion time scale is changed. Increasing the azimuthal grid points is difficult because the time step is limited by the CFL condition that becomes short, and computational cost becomes huge. Nevertheless, we have resolved the nonaxisymmetric structure with mode number $m = 1$. It will be our future work to increase the number of azimuthal grid points.

In this paper, we have not included the outer cold disk because the accretion time scale from the cold disk is longer than the time scale of our simulation. To simulate the transition without abruptly including the radiative cooling, it is preferable to simulate the transition by increasing the mass accretion rate from the outer cold disk. It will also be our future work to include the outer cold disk.

We thank Mami Machida, Tomohisa Kawashima, Tomoyuki Hanawa, Hideyuki Hotta, and Hirofumi Noda for discussions. This work has been supported in part by JSPS KAKENHI 16H03954(PI RM), 20H01941(PI RM), 17H01102A(PI KO), 18K03710(PI KO), JSPS Grant-in-Aid for Young Scientists (17K14260 H.R.T.), and MEXT “Priority Issue on Post-K Computer (Elucidation of the Fundamental Laws and Evolution of the Universe).” Numerical simulations were performed using the XC50 at the Center for Computational Astrophysics, National Astronomical Observatory of Japan.

REFERENCES

- Abramowicz, M. A., Chen, X., Kato, S., Lasota, J.-P., & Regev, O. 1995, *ApJ*, 438, L37
- Arnaud, K. A., Branduardi-Raymont, G., Culhane, J. L., et al. 1985, *Monthly Notices of the Royal Astronomical Society* (ISSN 0035-8711), 217, 105
- Blumenthal, G. R., Lin, D. N. C., & Yang, L. T. 1984, *ApJ*, 287, 774
- Dedner, A., Kemm, F., Kröner, D., et al. 2002, *Journal of Computational Physics*, 175, 645
- Denney, K. D., De Rosa, G., Croxall, K., et al. 2014, *ApJ*, 796, 134
- Done, C., Davis, S. W., Jin, C., Blaes, O., & Ward, M. 2012, *MNRAS*, 420, 1848
- Drury, L. O. 1985, *MNRAS*, 217, 821
- Fender, R. P., Belloni, T. M., & Gallo, E. 2004, 355, 1105
- González, M., Audit, E., & Huynh, P. 2007, *A&A*, 464, 429
- Hawley, J. F. 2000, *ApJ*, 528, 462
- Hawley, J. F., & Balbus, S. A. 2002, *ApJ*, 573, 738
- Husemann, B., Urrutia, T., Tremblay, G. R., et al. 2016, *A&A*, 593, L9
- Jiang, Y.-F., Blaes, O., Stone, J. M., & Davis, S. W. 2019a, *ApJ*, 885, 144
- Jiang, Y.-F., Stone, J. M., & Davis, S. W. 2019b, *ApJ*, 880, 67
- Jin, C., Done, C., & Ward, M. 2020, *MNRAS*, 495, 3538
- Kato, S. 1978, *MNRAS*, 185, 629
- . 1987, *PASJ*, 39, 645
- . 2001, *PASJ*, 53, L37
- . 2016, *Oscillations of Disks: Astrophysics and Space Science Library*, Springer Japan, Vol. 437, doi:10.1007/978-4-431-56208-5
- Kato, Y., Mineshige, S., & Shibata, K. 2004, *ApJ*, 605, 307
- Kobayashi, H., Ohsuga, K., Takahashi, H. R., et al. 2018, *PASJ*, 70, 22
- LaMassa, S. M., Yaqoob, T., & Kilgard, R. 2017, *ApJ*, 840, 11
- LaMassa, S. M., Cales, S., Moran, E. C., et al. 2015, *ApJ*, 800, 144
- Lowrie, R. B., Morel, J. E., & Hittinger, J. A. 1999, *ApJ*, 521, 432
- Machida, M., Hayashi, M. R., & Matsumoto, R. 2000, *ApJL*, 532, L67
- Machida, M., & Matsumoto, R. 2008, *PASJ*, 60, 613
- Machida, M., Matsumoto, R., & Mineshige, S. 2001, *PASJ*, 53, L1
- Machida, M., Nakamura, K. E., & Matsumoto, R. 2006, *PASJ*, 58, 193
- MacLeod, C. L., Ross, N. P., Lawrence, A., et al. 2016, *MNRAS*, 457, 389
- Mahmoud, R. D., & Done, C. 2018, *MNRAS*, 480, 4040
- . 2020, *MNRAS*, 491, 5126
- Manmoto, T., Kato, S., Nakamura, K. E., & Narayan, R. 2000, *ApJ*, 529, 127
- Matsumoto, Y., Asahina, Y., Kudoh, Y., et al. 2019, *PASJ*, 71, 83
- Mishra, B., Fragile, P. C., Johnson, L. C., & Kluźniak, W. 2016, *MNRAS*, 463, 3437

- Miyoshi, T., & Kusano, K. 2005, *Journal of Computational Physics*, 208, 315
- Narayan, R., Yi, I., & Mahadevan, R. 1995, *Nature*, 374, 623
- Noda, H., & Done, C. 2018, *MNRAS*, 480, 3898
- Noda, H., Makishima, K., Yamada, S., et al. 2014, *ApJ*, 794, 2
- Noda, H., Minezaki, T., Watanabe, M., et al. 2016, *ApJ*, 828, 78
- Oda, H., Machida, M., Nakamura, K. E., & Matsumoto, R. 2009, *ApJ*, 697, 16
- Oda, H., Machida, M., Nakamura, K. E., Matsumoto, R., & Narayan, R. 2012, *Publications of the Astronomical Society of Japan*, 64, 15
- Ohsuga, K., & Mineshige, S. 2011, *ApJ*, 736, 2
- Ohsuga, K., Mineshige, S., Mori, M., & Kato, Y. 2009, *PASJ*, 61, L7
- Oknyansky, V. L., Winkler, H., Tsygankov, S. S., et al. 2019, *MNRAS*, 483, 558
- Oknyansky, V. L., Gaskell, C. M., Huseynov, N. A., et al. 2017, *MNRAS*, 467, 1496
- Paczyński, B., & Wiita, P. J. 1980, *A&A*, 88, 23
- Papaloizou, J. C. B., & Pringle, J. E. 1984, *MNRAS*, 208, 721
- Parker, M. L., Scharrel, N., Grupe, D., et al. 2019, *MNRAS*, 483, L88
- Petrucci, P. O., Ursini, F., De Rosa, A., et al. 2018, *A&A*, 611, A59
- Quataert, E., & Gruzinov, A. 2000, *ApJ*, 539, 809
- Sadowski, A., & Narayan, R. 2015, *MNRAS*, 453, 3213
- Shakura, N. I., & Sunyaev, R. A. 1973, *A&A*, 24, 337
- Shappee, B. J., Prieto, J. L., Grupe, D., et al. 2014, *ApJ*, 788, 48
- Sniegowska, M., Czerny, B., Bon, E., & Bon, N. 2020, *A&A* in press, arXiv:2007.06441
- Suresh, A., & Huynh, H. T. 1997, *Journal of Computational Physics*, 136, 83
- Takahashi, H. R., & Ohsuga, K. 2013, *ApJ*, 772, 127
- Takahashi, H. R., Ohsuga, K., Kawashima, T., & Sekiguchi, Y. 2016, *ApJ*, 826, 23
- Takahashi, H. R., Ohsuga, K., Sekiguchi, Y., Inoue, T., & Tomida, K. 2013, *ApJ*, 764, 122
- Tsang, D., & Lai, D. 2009, *MNRAS*, 393, 992
- Turner, T. J., & Pounds, K. A. 1989, *Monthly Notices of the Royal Astronomical Society (ISSN 0035-8711)*, 240, 833
- Wu, X.-B., Li, Q.-B., Zhao, Y.-H., & Yang, L.-T. 1995, *ApJ*, 442, 736
- Yang, L. T., Wang, D. X., Wu, S. P., & Liu, Z. D. 1995, *A&A*, 303, 635
- Yokoyama, T., & Shibata, K. 1994, *ApJ*, 436, L197